
This is an electronic reprint of the original article.
This reprint may differ from the original in pagination and typographic detail.

Mekgwe, Gadifele Nicolene; Akinribide, Ojo Jeremiah; Akinwamide, Samuel; Olubambi, Peter Apata

Densification and corrosion properties of graphite reinforced binderless TiC70N30 ceramic composites

Published in:
Journal of the European Ceramic Society

DOI:
[10.1016/j.jeurceramsoc.2024.04.028](https://doi.org/10.1016/j.jeurceramsoc.2024.04.028)

Published: 01/09/2024

Document Version
Publisher's PDF, also known as Version of record

Published under the following license:
CC BY

Please cite the original version:
Mekgwe, G. N., Akinribide, O. J., Akinwamide, S., & Olubambi, P. A. (2024). Densification and corrosion properties of graphite reinforced binderless TiC70N30 ceramic composites. *Journal of the European Ceramic Society*, 44(11), 6223-6238. <https://doi.org/10.1016/j.jeurceramsoc.2024.04.028>

This material is protected by copyright and other intellectual property rights, and duplication or sale of all or part of any of the repository collections is not permitted, except that material may be duplicated by you for your research use or educational purposes in electronic or print form. You must obtain permission for any other use. Electronic or print copies may not be offered, whether for sale or otherwise to anyone who is not an authorised user.



Densification and corrosion properties of graphite reinforced binderless TiC₇₀N₃₀ ceramic composites

Gadifele Nicolene Mekgwe^{a,*}, Ojo Jeremiah Akinribide^a, Samuel Olukayode Akinwamide^{a,b}, Peter Apata Olubambi^a

^a Centre for Nanomechanics and Advanced Materials, School of Mining, Metallurgy and Chemical Engineering, University of Johannesburg, South Africa

^b Department of Mechanical Engineering, Aalto University, Espoo, Finland

ARTICLE INFO

Keywords:

TiCN ceramic composites
Graphite
Corrosion resistance
Spark plasma sintering

ABSTRACT

In this study, binderless TiC₇₀N₃₀ ceramic composites with varying graphite (TiC₇₀N₃₀-Gr) reinforcements were fabricated via spark plasma sintering and their effect on densification was assessed. Subsequently, the electrochemical behaviour of TiC₇₀N₃₀-Gr composites was evaluated in 0.5 mol/L hydrochloric acid (HCl), 0.5 mol/L sulphuric acid (H₂SO₄) and 0.5 mol/L nitric acid (HNO₃) solutions using open circuit potential, potentiodynamic polarization and electrochemical impedance spectroscopy (EIS) methods. The corrosion behaviour of TiC₇₀N₃₀-based ceramic composites with and without graphite reinforcement exhibited high corrosion resistance in the acidic electrolytes. Composites with 0.5 and 1.0 wt% graphite content showed lower I_{corr} values of 0.452 μA and 0.081 μA in 0.5 mol/L HCl and 0.5 mol/L HNO₃, respectively, while specimen without graphite addition showed better corrosion resistance in 0.5 mol/L H₂SO₄ (0.041 μA). Based on the corrosion results, the corrosion properties of TiC₇₀N₃₀ ceramic composites in HCl and HNO₃ solutions were significantly enhanced upon the incorporation of graphite reinforcements. However, the corrosion test results conducted in H₂SO₄ solution showed that the addition of graphite had a negligible influence on the corrosion resistance of the titanium carbonitride (TiCN) composites.

1. Introduction

Transition metal carbides and nitrides have become one of the most prolific materials in advanced technological industries particularly as cutting tools and modern surface protection. TiCN ceramic based composite is abundant, thus exhibit economic viability for various industrial application and has indicated great competencies required for application in harsh conditions owing to the combined superior properties such as high corrosion, oxidation and wear resistance coupled with extremely high melting point, chemical inertness, and high temperature hardness [1–4]. When compared to tungsten carbide-cobalt (WC-Co), TiCN has several potential advantages due to increased hardness, high edge strength and edge sharpness [5–8]. Nowadays, this material has acquired tremendous attention from material scientists, ceramicists, and researchers worldwide and possess potential utilization in mechanical pump seals, waterjet nozzle, sliding wear resistant parts and molding core and other various industrial sectors. TiCN based composites are widely applied on various material via coating techniques to improve

their functional corrosion properties [9–12].

Metallic binders such as Iron (Fe), Co and/or nickel (Ni) are conventionally incorporated into the hard phase of TiCN to improve wettability, toughness and solubility between the metal and the ceramic phase [13–15]. However, owing to the substantial dissimilar materials exhibited by cermets, variance in electrode potential between the hard phase and binder phase causes the material to be prone to micro galvanic corrosion in chemically aggressive environments [16,17]. Also, because of the non-uniform structure as components dissolve, inverse passivation is contingent on the electrolyte composition. Fe and Ni has demonstrated potential shift to the passive region which makes these metallic binders corrosion resistant as opposed to Co which usually dissolve in an active state [18]. Electrochemical method has proved to a greater extend beneficial to evaluate corrosion resistance of TiCN based cermets as compared to immersion experiments and studies with various electrolytes are reported in literature to examine the corrosion reaction morphology and determine the corrosion rate to mimic the actual working conditions.

* Corresponding author.

E-mail address: nicolenemekgwe@gmail.com (G.N. Mekgwe).

<https://doi.org/10.1016/j.jeurceramsoc.2024.04.028>

Received 24 January 2024; Received in revised form 1 April 2024; Accepted 11 April 2024

Available online 12 April 2024

0955-2219/© 2024 The Authors. Published by Elsevier Ltd. This is an open access article under the CC BY license (<http://creativecommons.org/licenses/by/4.0/>).

Xu et al. [19] studied the effect of Ni content and different Ni/Co ratios on corrosion resistance of TiCN based cermets under acidic and alkaline environments (1 M of HCl and 1 M of NaOH). Cermet with 1 and 3 ratio of Ni/Co showed excellent corrosion resistance in both media, confirming that Ni content is beneficial to improve corrosion resistance of the cermet. The enhanced corrosion resistance of cermet in 1 M NaOH solution can be ascribed to a dense passive film oxidized from binder phase, passivation current was substantially reduced, and the passivation range expanded with Ni addition. Using hot isostatic pressing (HIP) sintering at 1500 °C for an hour, the effect of ruthenium on the electrochemical behaviour of TiCN based cermet in 1 mol/L HCl solution has been reported. 0.5 % and 1.0 % Ru demonstrated enhanced corrosion resistance properties whereas excess Ru (1.5 wt%) content exhibited poor corrosion properties due to the existence of pores and caused the surface to suffer from micro galvanic attack in H₂SO₄ solution and deteriorates corrosion resistance properties of the cermet [20]. Wan et al. [21] studied the effect of Cr₃C₂ addition on the corrosion properties of TiCN-Mo₂C-Ni based cermet in 2 mol/L HNO₃ acid environment. The corrosion resistance of the binder phase was enhanced as the Cr₃C₂ addition increased and this was due to the formation of the reticulate binder phase on the corrosion surface of the cermet. Ti (C, N)-based cermets were prepared, with TiC_{0.7}N_{0.3} / (Ti_{0.88}W_{0.12}) C mass fraction ratio of 4:5 and 16:5 by HIP furnace at 1480 °C for an hour. Using H₂SO₄ (pH = 1) and NaOH (pH = 13) solutions, higher Ti (C, N)/Ti₂WC fraction showed improvement in both solutions [6].

Chen et al. [16] investigated the corrosion resistance of Ti (C, N)-Ni/Cr cermets in 0.2 m/L H₂SO₄ solution. The cermets were prepared by vacuum sintering at 1718 K for an hour and the cermets exhibited 3 passive regions with various passive current densities. The first region was due to the formation of TiO_x while the second was attributed to the Ni content. The authors further stated that the introduction of Cr addition enhanced the passivation behaviour of the cermet. NiCr addition has shown great performance and improvement on the current density of the cermet as compared to minimal influence demonstrated by Cr₃C₂ addition in 1 mol/L HNO₃ [22]. The NiCr content accelerate sufficient and stable chromium oxide film layer formation which hinders the progression of binder phase corrosion in acid solution and the corrosion resistance of the cermet was enhanced as the content of dissolved Cr atoms decreased.

The literature reports methods to mitigate the vulnerability of the binder phase in chemically aggressive environments by modifying the composition and incorporating various corrosion resistant reinforcements to further enhance the corrosion properties of the cermets. However, the substantial distinct corrosion potentials of the ceramic phase and metal phase cannot be ignored. Currently, the limitations of binder addition into the ceramic phase have urged the importance to fabricate binderless TiCN based ceramic composites for optimal performance during application. Lavrenko et al. [23] fabricated TiC_{0.5}N_{0.5} at 1630–1850 °C, 195 MPa for 60–90 min via HIP sintering method without additives and demonstrated outstanding corrosion resistance in 3 % NaCl electrolyte at 20 °C. The electrochemical resistance of TiC_xN_y ceramic based composites developed by pulsed electric current sintering in 3.5 wt% NaCl solution is reported [24]. Ceramics with 50/50 TiC/TiN composition exhibited enhanced corrosion resistance in severe chloride ions as compared to other ceramics used in the study. Although ceramic based materials are considered to be highly resistant to corrosion, it is of utmost importance that the corrosion resistance of these materials is meticulously investigated. To, limited research has been reported on the electrochemical corrosion resistance of binderless TiC₇₀N₃₀ based ceramic reinforced by carbon-based material.

In this study, spark plasma sintering (SPS), an advanced sintering technology was employed to fabricate binderless TiC₇₀N₃₀ ceramics composites with varying graphite ratios (wt%). The effect of graphite content on the microstructure and densification behaviour of TiCN ceramic was investigated to determine the ceramic composition with optimal properties. Subsequently, solutions of 0.5 mol/L HCl, 0.5 mol/L

H₂SO₄ and 0.5 mol/L HNO₃ were used as acidic corrosive media to simulate typical aggressive environments where corrosion by chloride ions, hydrogen ions and the severe oxidability simultaneously occur.

2. Materials and methods

2.1. Materials characterization and preparation

The as-received powders utilized in this study were TiC₇₀N₃₀ (average particle size, 1.0–1.3 μm; purity 99.5 %), supplied by H.C. Starck, Germany and graphite (average particle size 1–2 μm; purity 99.9 %), sourced from Sigma-Aldrich South Africa. The morphology and composition of the starting powders were examined using a scanning electron microscope (Model: FE-SEM; JSM-7900F) from JEOL equipped with energy-dispersive X-ray spectrometer (SEM/EDS). Particle size distribution and volume density (Table 1) of the starting powders were evaluated using laser diffraction (Malvern particle size analyzer, Mastersizer 2000) with deionized water as a dispersant. Moreover, varying compositions of different powders consisting of TiC₇₀N₃₀ and graphite in weight fractions (wt%) were poured into a 250 ml plastic container filled up to 20 % of its capacity with WC balls. The container was then axially loaded and subjected to both rotational and translational motion in a T2F Turbula shaker mixer operating at ambient temperature and a speed of 101 rpm for 4 h.

2.2. Consolidation of admixed powders

The admixed powders were uniaxially pressed in a 40 mm graphite die lined with graphite foils, using two graphite punches to minimize heat loss due to radiation. After cold compaction, the samples were sintered using the SPS system (model HHPD-25) from FCT, Germany at a sintering temperature of 2100 °C, heating rate of 100 °C/min, dwelling time of 10 min under a pressure of 50 MPa. The sintering temperature was continually measured by an optical pyrometer implanted at 3 mm from the centre of the sintered sample. The sintered compacts were sand blasted to remove the graphite foils after the sintering process. Successively, the densification of the sintered compacts was examined using Archimedes' principle. The relative density was calculated with reference to the theoretical density of the admixed powders using the rule of mixture (Table 2).

2.3. Metallography, microstructural analysis, and grain size measurement

The sintered specimens were sectioned and prepared for microstructural analysis using standard grinding and polishing metallographic procedure as stipulated by ASTM standard. The surface of the specimens was ground using Aka-Piatto 120 and Aka-Allegran 9 grinding discs. Polishing was performed with Aka-Daran polishing clothes with Dia-Maxx 3 μm poly and fumed silica 0.2 μm suspensions. Krolls reagent (50 ml distilled water, 10 ml HF and 40 ml HNO₃) was employed to for 30 s to identify the grains and boundaries, as well as to obtain precise microstructures. Following the etching procedure, the microstructural evolution and composition of the sintered TiCN-Gr ceramic composites were examined using SEM (FE-SEM JOEL JSM-7900F) equipped with an energy-dispersive spectroscopy (EDS) detector.

2.4. Electrochemical tests

The corrosion resistance of the specimens was investigated in three

Table 1
Particle size distribution of as-received powders.

Average μm	Dv [50] (μm)	Dmin (μm)	Dmax (μm)	Daverage (μm)
TiC ₇₀ N ₃₀	3.19	0.04	20.00	2.50
Graphite	7.35	0.80	40.00	10.00

Table 2

Theoretical and relative densities of graphite reinforced TiCN ceramic composites.

Ceramic composition	Theoretical density (g/cm ³)	Measured density (g/cm ³)	Relative density (%)
A. TiC ₇₀ N ₃₀ -0 wt% Gr	5.02	4.91	97.8
B. TiC ₇₀ N ₃₀ -0.5 wt % Gr	4.99	4.92	98.6
C. TiC ₇₀ N ₃₀ -1.0 wt % Gr	4.95	4.93	99.6
D. TiC ₇₀ N ₃₀ -1.5 wt % Gr	4.92	4.83	98.2

acidic corrosive media containing 0.5 mol/L HCl, 0.5 mol/L H₂SO₄ and 0.5 mol/L HNO₃ solutions. A VersaSTAT 4 potentiostat equipped with Versastudio software (Model 22382, Princeton Applied research, USA) was used to perform the tests. Prior to potentiodynamic polarization, an open circuit potential test was conducted for 2 h to ensure adequate stabilization of the specimens in the test environments. The experiments were conducted at room temperature using a standard 3-electrode cell with TiCN-Gr samples as the working electrode, a graphite rod as the counter electrode, and Ag/AgCl₂ electrode filled with aqueous 3 M KCl solution as reference electrode. Potentiodynamic polarization studies were carried out by scanning from initial to final potentials of -1.5 mV and 1.5 mV, respectively, at a scan rate of 0.2 mV/s. Moreover, the samples were analyzed using the electrochemical impedance spectroscopy (EIS) method to determine the charge transfer between the specimen surface and test electrolytes at an initial and final frequency of 100 KHz and 0.01 Hz respectively.

3. Results and discussion

3.1. SEM micrographs and particle size distribution of as-received powders

The scanning electron microscopy (SEM) images, EDS mapping and spectrum of the as-received powders are shown in Fig. 1. The particle morphology of TiC₇₀N₃₀ demonstrate distinct three-dimensional irregular shaped particles with edgy hard angles, and relatively equiaxed particles uniformly dispersed. On the other hand, the graphite particles exhibit a flaky or platy like morphology. The coalescence of the TiC and TiN particles evident in the morphology of the TiC₇₀N₃₀ can promote homogenization and improve densification during the sintering process [25]. The particle sizes of the starting powders are analysed in terms of differential mass-weighted distribution using a 50 % mass distribution (Dv [50]). The TiC₇₀N₃₀ and graphite powders recorded average particle sizes of 3.19 μm and 7.35 μm, respectively as displayed in Table 1. Further analysis of the powders, according to Fig. 2, using cumulative frequency volume distribution method shows that the TiC₇₀N₃₀ and graphite powders have average particle sizes of 2.5 μm and 10 μm, respectively. The minimum and maximum particle sizes of the powders are also presented in Table 1.

3.2. Densification behaviour during spark plasma sintering of graphite reinforced TiCN ceramic composites

Analyzing the sintering profiles is crucial for understanding the process and densification of binder-less TiCN powder during sintering and provides valuable insight into the behavior spark plasma sintered compacts. Fig. 3 illustrates the time vs temperature profile of the TiC₇₀N₃₀-Gr composites. The temperature curve commenced from 250 °C as the sensitivity of the thermocouple employed in monitoring the temperature of the samples within the sintering assembly required this initial heating. Subsequently, the specimens were gradually heated to

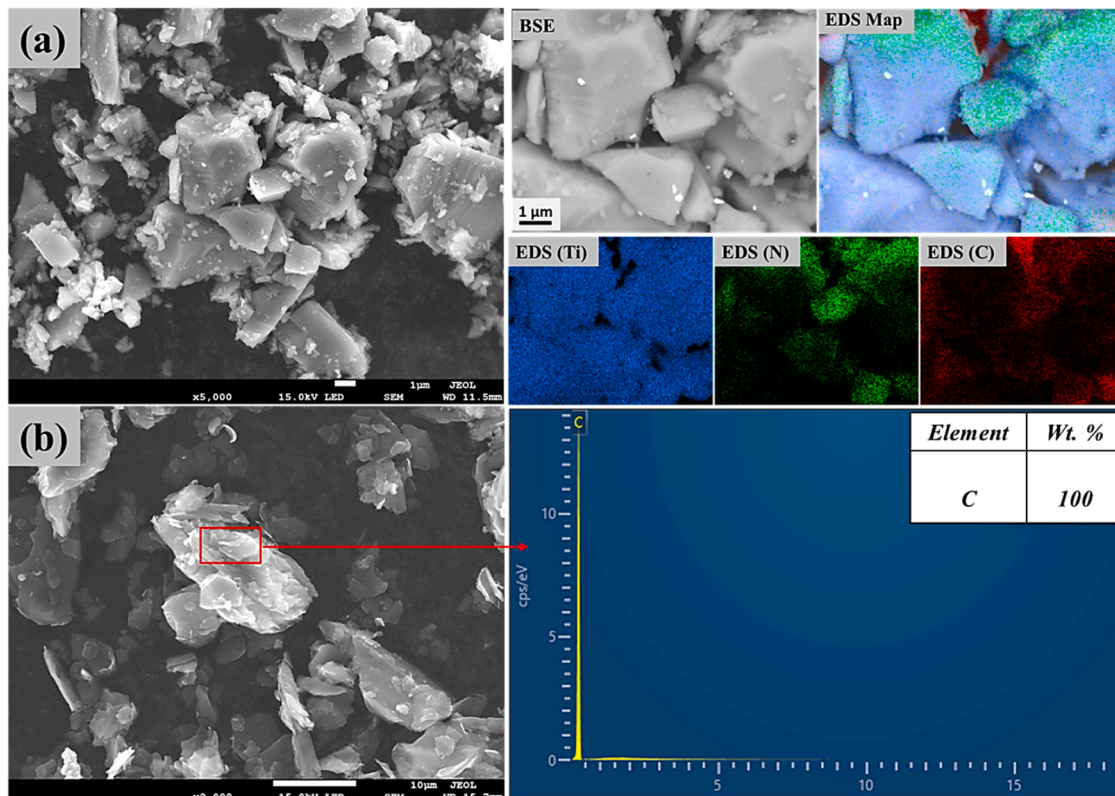


Fig. 1. SEM morphology and corresponding EDS of (a) TiC₇₀N₃₀ and (b) Graphite.

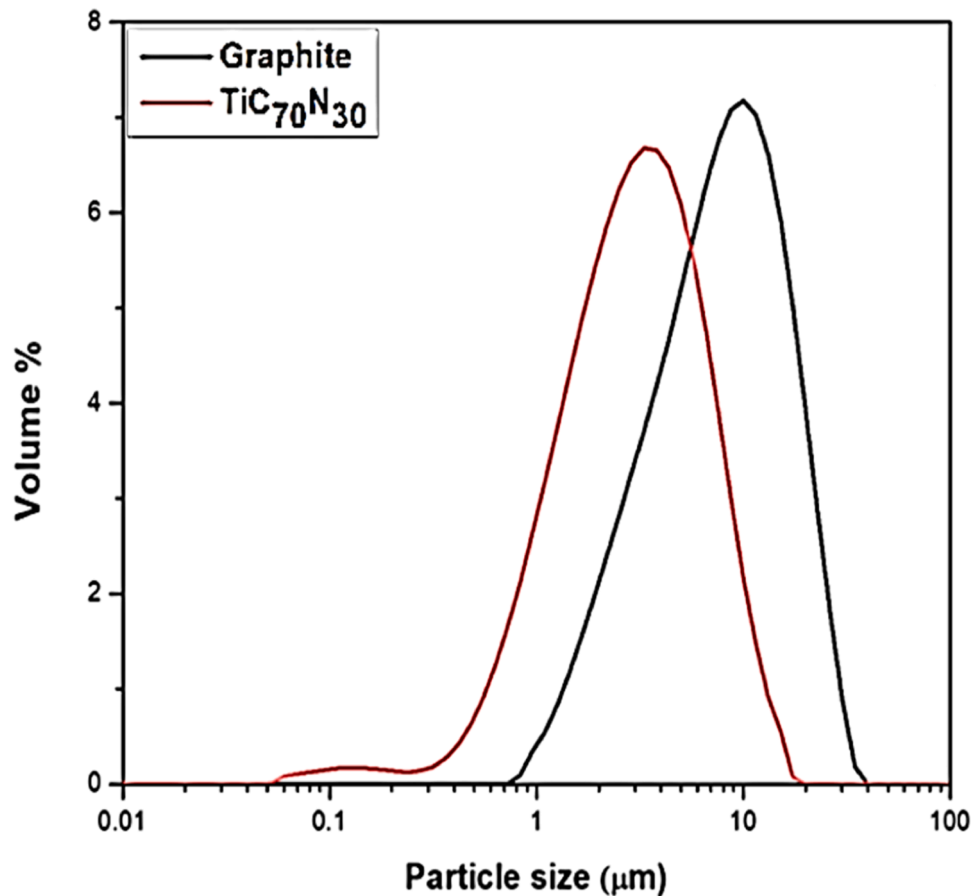


Fig. 2. Particle size distribution of as-received powders.

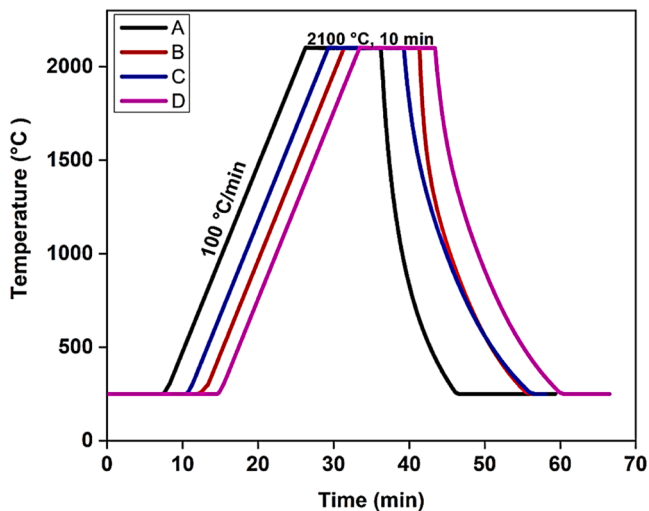


Fig. 3. Spark plasma sintering profiles between time and temperature of the sintered TiCN-Gr ceramics during consolidation.

the final sintering temperature of 2100 °C at a heating rate of 100 °C/min and held for about 10 min during which full densification was achieved. The curve shows similar patterns for all the sintered specimens presented in the sintering profile. However, the time taken for 40 mm diameter with 5 mm thickness sintered compacts of TiCN samples with graphite reinforcement varies among the specimens. From the graph, it is observed that the specimen without graphite reinforcement (sample A) reached the sintering temperature in approximately 26 min, followed

by sample with 1.0 wt% graphite addition (29 min) while the samples with 0.5 and 1.5 wt% graphite addition took 31 min and 33 mins, respectively. Furthermore, the time taken for the samples to complete sintering varies slightly, ranging from range 56–66 min with increased graphite addition. It can be concluded that overall densification of the sintered compacts is dependent on the sintering time adopted for consolidation of the powders, and a similar observation was reported in a recent study by Guillard et al. [26].

The data obtained during sintering was used to plot the graphs of temperature and displacement against time (Fig. 4). It is evident that the displacement increased with increasing sintering temperature, denoting good reproducibility during SPS of graphite reinforced binderless ceramics composites. A similar trend was observed for all the sintered specimens, suggesting consistent behavior across samples. It is worth noting that the increased temperature also promotes diffusion mechanism and mass transportation among the graphite and TiC₇₀N₃₀ powder particles. This results in punch displacement, further promoting bulk deformation, compaction, and necking [27] [28]. Moreover, the piston displacement provides justification for the thermal expansion of graphite punches. As observed, the samples showed three turning points, corresponding to the stages seen in Fig. 5. The graphs also show large displacement, indicating better densification. In the first turning point, the temperature is proportional to the displacement, indicating compression and softening of the powder precursor [29]. The second turning point corresponds to the highest densification during the holding period, where the isothermal temperature was constant for 10 mins. During this stage, interdiffusion of elements occurs, and the pores closes, leading to the formation of the final microstructure [26,30]. The third turning represents the cooling stage, during which the displacement increases due to shrinkage [31]. Moreover, larger punch displacements of 7.88 mm, 7.75 mm, 6.76 mm and 6.87 mm were observed for

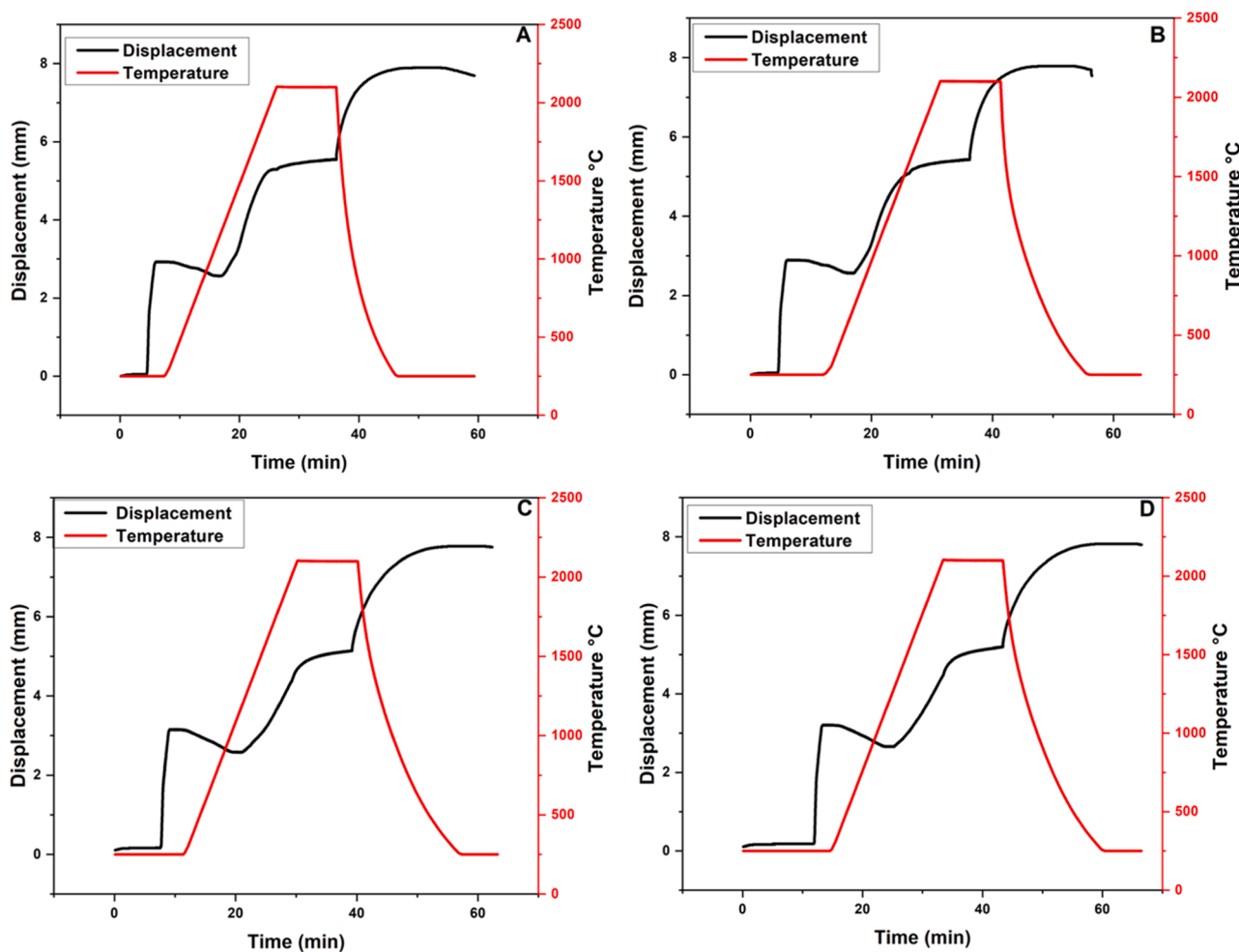


Fig. 4. Displacement and temperature as a function of time for $\text{TiC}_{70}\text{N}_{30}$ sintered compacts: (A) 0 wt%, (B) 0.5 wt%, (C) 1.0 wt% and (D) 1.5 wt% graphite addition.

specimen A, B, C and D respectively. The ceramic composite without graphite addition (Fig. 4A) showed the highest punch displacement, which gradually decreased with increased graphite content.

The displacement rate shows the densification mechanism during the SPS process and can be used as a standard to illustrate the progression of the sintering process. The plots of displacement as a function of sintering time for the sintered compacts are presented in Fig. 5. From Fig. 5a, the ceramic composites are seen to display similar displacement behavior, with three distinct peak areas on the displacement rate axis representing three main sintering stages. The first peak can be attributed to the initial rearrangement of the $\text{TiC}_{70}\text{N}_{30}$ and graphite powder particles, facilitated by minimum pressure and gas removal, often accompanied by spark creation. This stage occurred within the first 17 minutes with displacement rates of 1.39 mm/min, 1.38 mm/min, 1.31 mm/min and 1.34 mm/min recorded by samples A, B, C and D, respectively. The minimal influence of graphite addition on the displacement rate suggests no significant deformation occurred, due to its high melting point ($\sim 3600^\circ\text{C}$) [32]. The second stage typically occurs between 18 and 36 min and is characterized by Joule heating effect and localized plastic deformation of the particles at contact points. This phase involves powder surface activation, partial formation of necks at contact points, atomic diffusion, and plastic flow [28,29]. The temperature is increased by Joule heating at the particle surface, leading to melting, evaporation and as a result of particle softening caused by bonding between the powders [33]. The third stage commences after 37 mins and continues until the end of the sintering process, during which the displacement rate reaches maximum density. A drastic reduction in the displacement

rate is observed in all the specimens due to the cooling of the SPS chamber to room temperature, and densification is completed by mass transportation as depicted in Fig. 5b (typical displacement curve for a sintering process). Overall, the highest densification rate is evident in specimen A, while specimen D exhibits the least densification rate due to its increased graphite content.

During sintering, rapid consolidation of distinct powder materials depends on the simultaneous application of high temperature, axial pressure, plasma combined with an electric current that passes through a powder. In contrast to hot pressing technology where pulsed currents are directly applied to the powder bed, serving as the heating source by the Joule effect [34]. The recorded current and current rate variations through the graphite punch against temperature during sintering are illustrated in Fig. 6. The applied current increases linearly with temperature and slightly decreased at a certain temperature when densification was achieved. The specimens are densified by the increased amount of electric current passing through the powders, leading to sufficient conductivity of the powder particles at the determined temperature. Hence, the applied heat becomes sufficient to allow diffusion bonding, resulting in a decrease in specimen resistance and heat dissipation [35]. The immediate decline in current could be attributed to punch displacement indicating densification completion. In accordance with the findings of Babapoor et al. [36], the flow of current through powder particles is significantly dependent on the electric conductivity of the powders [36]. As observed in Fig. 6a, specimens A, B and D showed maximum electric currents of 4.98 kA, 4.56 kA and 4.48 kA respectively, within the temperature range of $1301 - 1374^\circ\text{C}$. However,

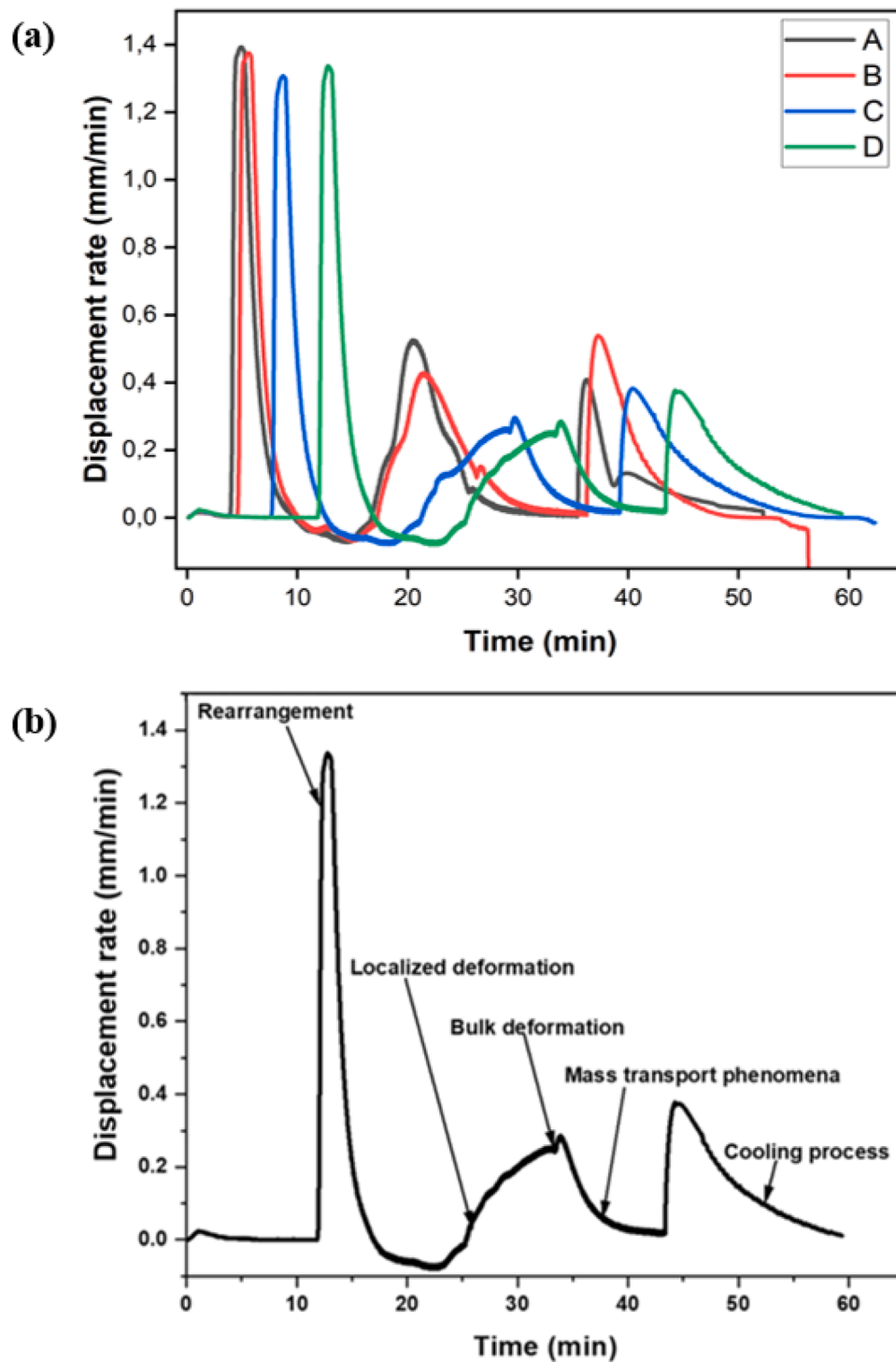


Fig. 5. (a) Displacement rate as a function of time showing stages of densification in sintered composites and (b) general densification mechanism during sintering.

specimen C displayed the least current variation in comparison with other composites, as it reached stability at a minimal electric current of 3.8 kA and temperature of 1780 °C. From Fig. 6b, the electric current ranged from 8 to 11 kA/s until the commencement of rapid punch displacement, after which it is reduced. This reduction clearly indicates an increase in the electric resistance of the powder.

The theoretical and final density of the as prepared TiCN-Gr ceramic composites as a function of weight % of graphite are shown in Fig. 7. The theoretical density of the composite was deduced from mass fraction and density of the components using rule of mixture equation:

$$P_{theoretical} = p_1w_1 + p_2w_2 \quad (1)$$

Whereby $P_{theoretical}$ is the theoretical density, p_1 and p_2 are the density and w_1 and w_2 are the weight fractions of the components of the two materials (TiC₇₀N₃₀ and graphite) respectively. The corresponding theoretical densities of the ceramic composites were 5.02 g/cm³, 4.99 g/cm³, 4.95 g/cm³ and 4.92 g/cm³ for composites A, B, C and D, respectively. This decrease in linear trend with increase in the weight fraction of graphite can be ascribed to the lower density of graphite (2.26 g/cm³) [32], consistent with the linear rule of mixture for

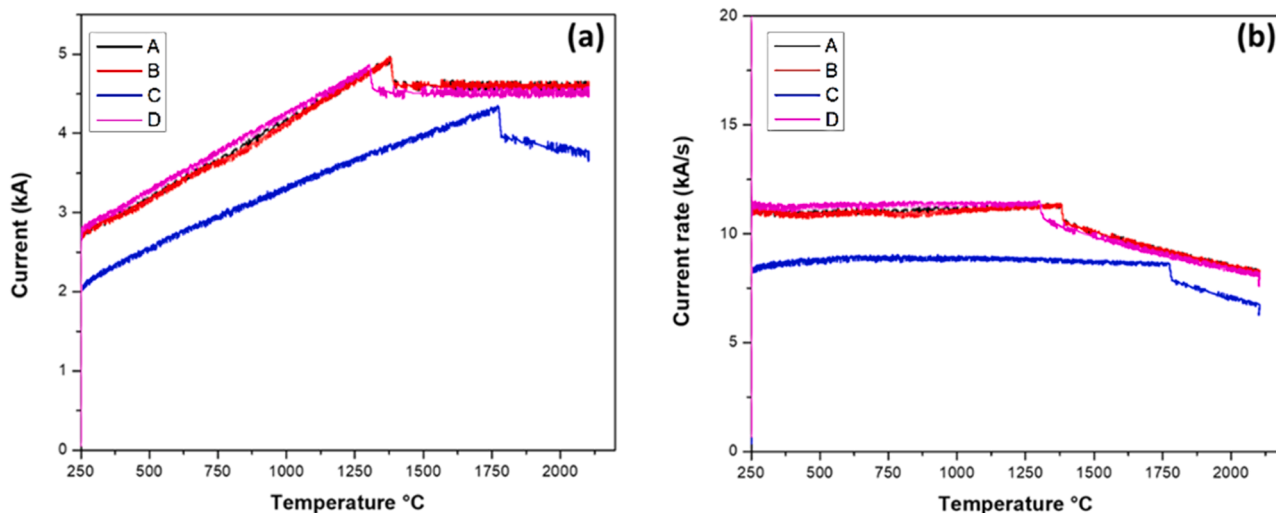


Fig. 6. Current and current rate as a function of temperature for spark plasma sintered TiC₇₀N₃₀-Gr ceramic compacts.

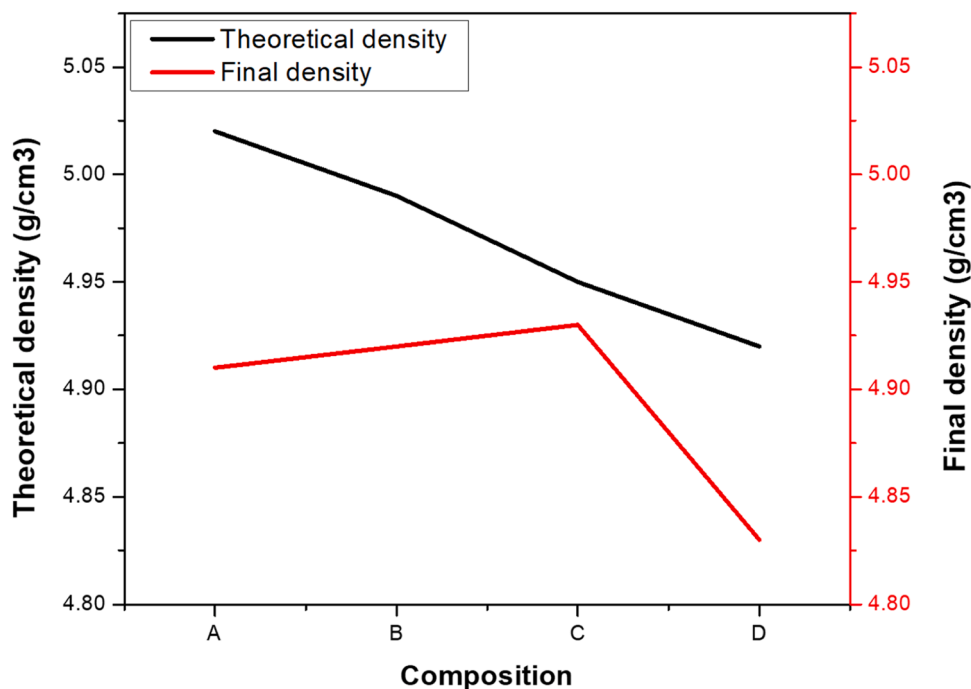


Fig. 7. Theoretical and Archimedes density of TiC₇₀N₃₀-Gr ceramic composites.

composites. However, the graph of the final density of the sintered compacts measured by Archimedes principle shows a dissimilar trend compared to the graph of theoretical density. The final density gradually increased as the graphite addition increased up to 1.0 wt% (specimen C). With excess graphite addition (1.5 wt%) the final density significantly decreased due to the observed increase in porosity caused by the widespread agglomerated graphite particles in the matrix, evident in the SEM micrographs presented in Fig. 8. The recorded relative densities exceeding 90 % in Table 2 demonstrate that full densification of pure TiCN can be accomplished with the SPS technology. Densification of pure and binderless TiCN with significant improvement in relative density has been reported in various SPS studies [25,37–39]. Moreover, this study reveals a noticeable improvement in relative density with increasing graphite addition from 0.5 to 1.0 wt%. This increase is indicative of enhanced densification and stronger bonding between TiCN particles and graphite. The relative density of the specimens

ranged from 97.8 % up to 99.6 % with slight variations, possibly attributed to the presence of pores observed in the microstructure. Notably, composition C showed the highest densification among all studied composition, which is advantageous for mechanical properties compared to other compositions. This superior densification of this specimen can be attributed to the homogenous dispersion of graphite particles within the matrix and the positive influence of the plasma generated during sintering. This facilitates the mobility and diffusion of the atoms through processes such as evaporation and melting of particle surfaces. These densification results confirm the effectiveness of SPS is an adequate technique for consolidating highly densified pure refractory ceramics without the need for sintering additives and binders.

3.3. Microstructural evolution

In Fig. 8, SEM micrographs of the sintered TiC₇₀N₃₀-Gr specimens,

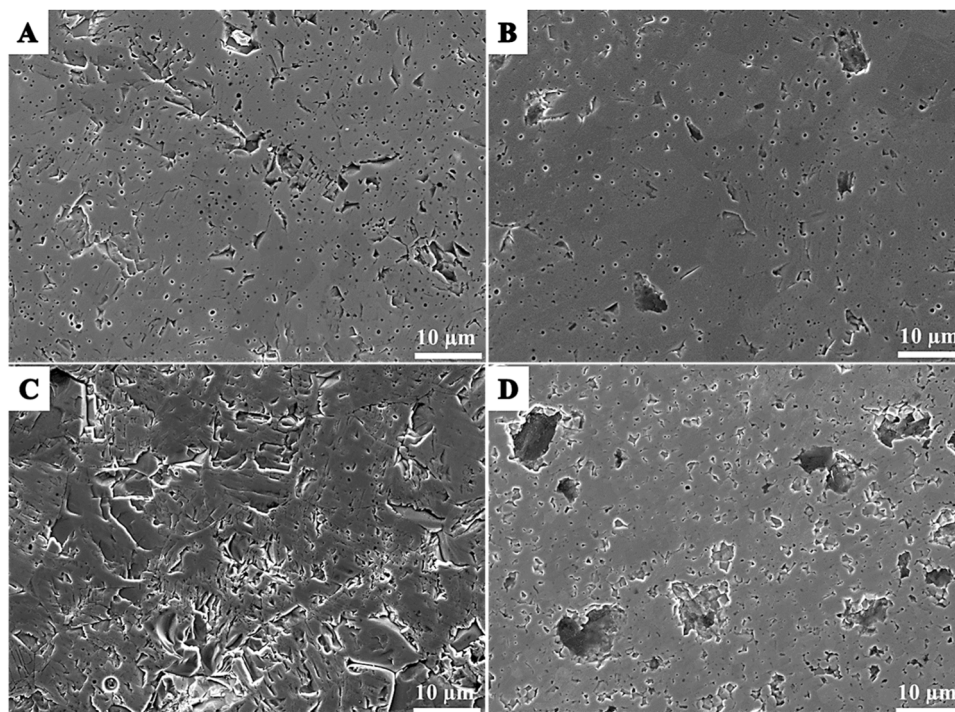


Fig. 8. SEM microstructures of the sintered $\text{TiC}_{70}\text{N}_{30}\text{-Gr}$ ceramic composites with (A) 0 wt%, (B) 0.5 wt%, (C) 1.0 wt% and (D) 1.5 wt% graphite addition.

provides understanding on the morphology and distribution of the ceramic hard phase. The specimens with and without graphite addition exhibit micropores; however, those with 0.5 and 1.5 wt% graphite addition show more pronounced intrinsic pores which can be attributed to the carbon rich phase. During sintering, gas entrapped due to reduction reactions is released, leading to micro-porosity on the composite surface, as reported in previous studies [40–43]. Nonetheless, in specimens with 0.5 and 1.5 wt% graphite (Figs. 8B and 8C), porosities evident can be attributed to non-uniform dispersion of graphite. During the later stages of sintering and the early phases of cooling, graphite particles did not fully dissolve but instead precipitated onto the TiCN particles. This phenomenon resulted in heterogeneous distributions, where graphite particles were unevenly dispersed within the ceramic matrix. The incomplete dissolution of graphite can be attributed to the reduced diffusion rate of graphite atoms into the carbonitride phase [44, 45]. Pores formed in binderless TiCN alloys fabricated via the SPS process have been attributed to grinding pull-out defects caused by the disparate hardness values between the very hard carbonitride phase matrix and the soft carbon-rich secondary phase. [25]. Therefore, graphite particles may contribute to particle pull-out from the microstructure during metallography preparation, thereby promoting micro porosity. It has been observed that both insufficient and excess carbon content can be detrimental to the properties of TiN and TiCN ceramic composites, a finding supported by existing literature. [43,46]. As observed in Table 2, the relative density of the sintered compact slightly increases with the addition of graphite up to 1.0 wt% and decreases with an excess amount of graphite (1.5 wt%). Specimen C, with 1.0 wt% graphite content, exhibited a homogenous and refined microstructure with minimal pore sizes compared to specimens B and D (Fig. 8D), which is crucial for enhancing mechanical properties. The presence of these pores could be attributed to the decomposition of TiCN and the release of nitrogen during sintering at high temperatures, hindering the dispersion of graphite particles within the composite. These findings suggest that graphite significantly influences the microstructure of the sintered ceramic composites under the selected experimental conditions.

To gain deeper insights and validate the observed microstructural

evolution depicted in Fig. 8, Backscattered Electron (BSE) micrographs were utilized to differentiate various phases based on their brightness, which is influenced by their average atomic numbers. Figs. 9 and 10 present SEM micrographs along with EDS elemental mapping and quantitative compositional analysis of sintered graphite reinforced TiCN ceramic composites containing 0.5 wt% (ceramic composite B) and 1.5 wt% (specimen D) graphite content, respectively. In Fig. 9, the elements constituting TiCN are represented accordingly, while a distinct dark phase, indicative of the secondary phase in the microstructure of the developed ceramic composites, is predominantly composed of graphite. The elemental weight percentages of Ti, C, and N are recorded as 77.6 %, 15.4 %, and 6.9 %, respectively. Fig. 10 reveals pronounced graphite segregation within the TiCN matrix due to undissolved graphite particles. The EDS analysis confirms that the dark regions are carbon-rich, attributed to the graphite reinforcement incorporated into the ceramic composites.

Fig. 11 presents the fracture morphology of spark plasma sintered $\text{TiC}_{70}\text{N}_{30}$ ceramic-based composites with varying graphite additions. Correlating with the results shown in Fig. 8, it is apparent that the incorporation of graphite has refined and modified the microstructure. According to Fig. 11A, the specimen without graphite exhibits visible pores, indicative of open porosity attributed to crack deflection, leading to increased energy absorption during fracture. Additionally, this porosity contributes to the reduced relative density of the material. The specimen reinforced with 0.5 wt% graphite shows a reduction in pore size, accompanied by a dull fracture surface characteristic of transgranular brittle fracture. With 1.0 wt% graphite content, the fracture morphology displays both ductile and cleavage features, attributed to the presence of uniformly distributed equiaxed grains and a refined microstructure. Conversely, the ceramic composite with 1.5 wt% graphite reinforcement exhibits a glassy transcrystalline microstructure, indicative of full cleavage fracture, along with a flatter surface attributed to coarse grains. Furthermore, grain refinement is observed with 1.0 wt% graphite reinforcement, showcasing an improved microstructure with uniformly dispersed grains compared to the ceramic composite with 1.5 wt% graphite, which demonstrates pronounced grain growth. In Figs. 11B and 11C, the introduction of graphite into the ceramic

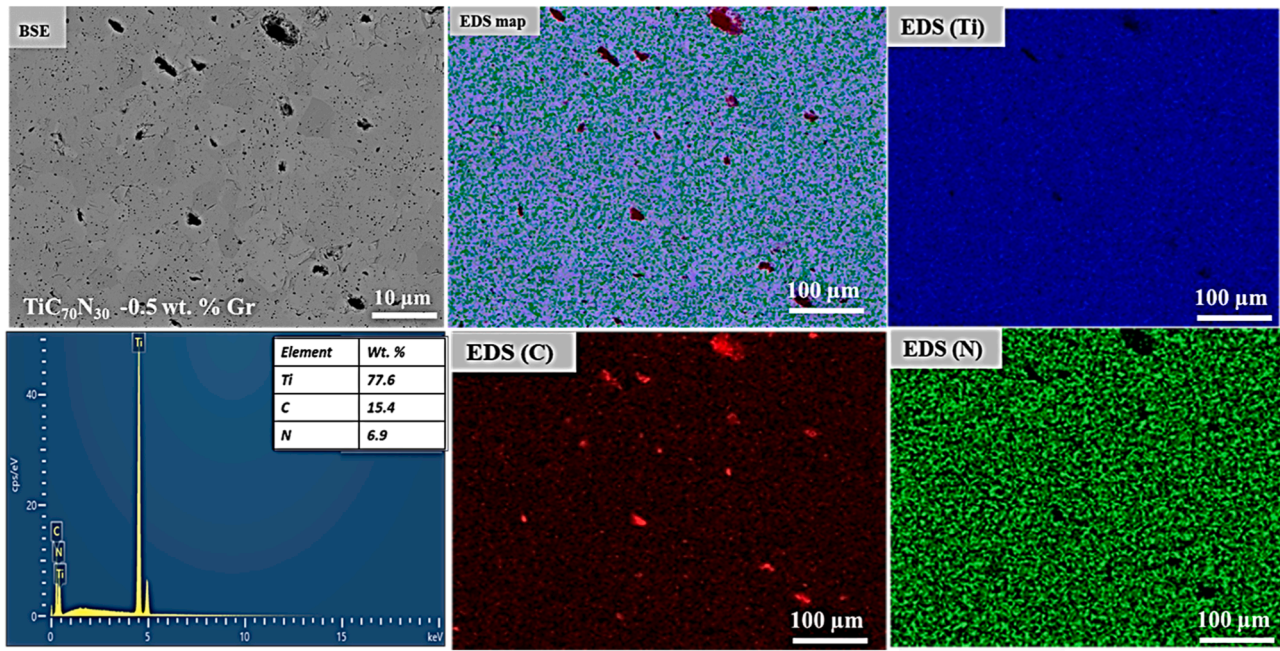


Fig. 9. SEM-EDS mapping of spark plasma sintered $\text{TiC}_{70}\text{N}_{30}$ -0.5 wt% Gr ceramic composite.

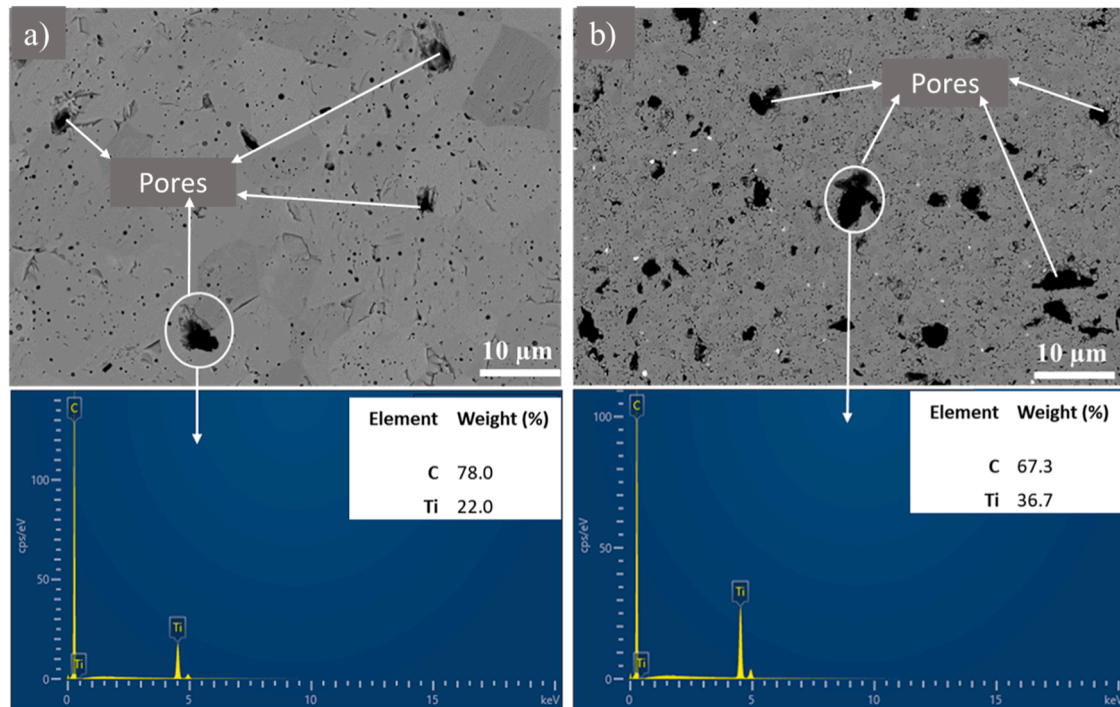


Fig. 10. BSE micrographs and EDS analysis of TiCN-Gr ceramic composites: a) 0.5 wt% Gr and b) 1.5 wt% Gr.

composites results in a noticeable reduction in pores, aligning with the relative densities recorded in Table 2. However, further examination reveals that excessive addition of graphite can adversely affect the microstructural characteristics of the sintered ceramic composites, potentially compromising their overall properties. However, an optimal balance must be struck to avoid adverse effects on microstructure and, consequently, material performance [47,48]. As the graphite content increased, porosity reduced but macro pores are clearly identified in the specimen with the highest graphite reinforcement (1.5 wt%). It has been proven that TiCN ceramic composites are characterized by

transcrystalline and intergranular fracture modes caused by the combination of coarse and fine microstructures respectively [39,49].

3.4. Electrochemical properties of binderless TiCN-Gr ceramic composites

The open circuit potential (E_{OCP}) for TiCN-Gr ceramic composites immersed in 0.5 mol/L HCL, 0.5 mol/L H_2SO_4 and 0.5 mol/L HNO_3 acidic electrolytes are shown in Fig. 12. Comparing the behaviour of these composites in different acidic electrolytes, specimen B demonstrate a more electropositive potential, which confirms its resistance to

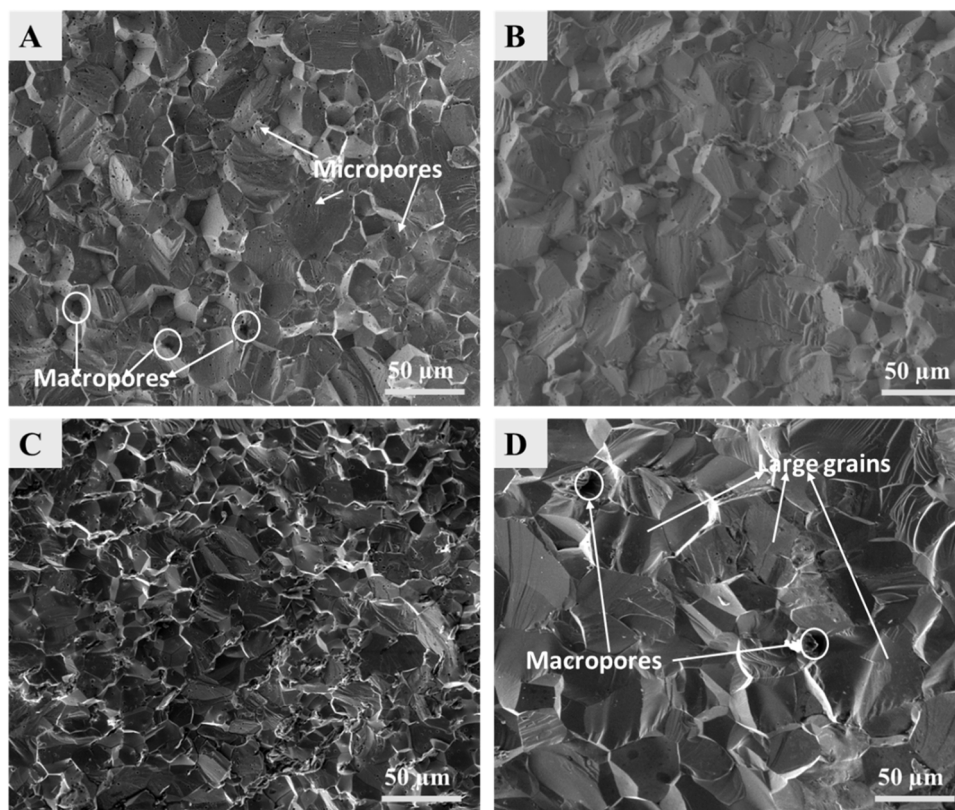


Fig. 11. SEM fracture morphology of the sintered $\text{TiC}_{70}\text{N}_{30}$ ceramic based composites with (A) 0 wt%, (B) 0.5 wt%, (C) 1.0 wt% and (D) 1.5 wt% graphite additions.

dissolution in both HCl and HNO_3 solutions compared to the other composites. However, for 0.5 mol/L H_2SO_4 solution, specimens B and D displayed E_{OCP} values of 0.372 V and 0.366 V, respectively. It is noteworthy that the shift in the potential of specimens A, C and D in a more electronegative direction necessarily depict poor corrosion rates. Rather, it confirms that specimen B is more thermodynamically stable in the test solutions. The gradual increase in potential shifting to a more noble direction at the beginning and then stabilizing over time, as observed in Fig. 12a and b, indicates the formation of a stable oxide layer (TiO_2) on the surface of the specimen. This oxide layer acts as a protective barrier against further corrosion. However, a different trend is observed in the HNO_3 electrolyte, where the E_{OCP} values gradually decrease with increased time. This behavior suggests the instability of the specimens due to the presence of aggressive ions in the electrolyte, which can disrupt the oxide layer and accelerate corrosion [23,52]. Furthermore, composites immersed in HNO_3 solution showed higher E_{OCP} values of 0.394 V, 0.450 V and 0.512 V for specimens A, D and B respectively, as compared to a lesser value of 0.2 exhibited by specimen C. Usually, higher positive of E_{OCP} value in materials denotes enhanced stability in corrosive medium [24,50]. TiCN-Gr exhibits good stability in acidic media, due to the presence of C-N and Ti-C-N active sites on the surface that support the release of hydrogen gas [51,52]. The distinct electronegativity and atomic radii between carbon and nitrogen atoms introduces active sites for hydrogen adsorption and the high activity of TiCN could be attributed to the presence of numerous substantial highly electrochemically active sites and crystalline framework. It is also important to note that the reaction between hydrogen atoms (from the HCl and HNO_3) and TiCN composites can alter the phase and structural composition of the composite. Furthermore, TiCN can undergo reversible hydrogen absorption and desorption processes in the presence of hydrogen, with the absorbed hydrogen (in form of TiH_2) being released upon heating at high temperatures [23,53,54]. Although carbon in TiCN-Gr ensures its stability in acidic media due to the formation of C-N and Ti-C-N active sites, carbon and nitrogen atoms can substitute each

other interchangeably in the TiCN lattice [55–57]. When carbon is substituted by N_2 , the relatively strong covalent nonmetallic Ti bond in TiC becomes weaker alongside the enhancement of covalent Ti-Ti bonds and ionization of the bond [58]. Therefore, an increase in carbon and nitrogen in their crystal structure reduces the chemical activity, which promotes the protective film at the surface of the material. The prolonged stability of these composites strongly suggests TiCN-Gr composites as suitable materials for use in corrosion-resistant applications.

The potentiodynamic polarization curves shown in Fig. 13 reveal the corrosion behavior of TiCN ceramic composites with varying graphite additions, while electrochemical parameters obtained through Tafel extrapolation are summarized in Table 3. These curves demonstrate dissimilar corrosion behavior in the acidic electrolytes, as evidenced by two distinct passive regions characterized by different passive current densities. The potentiodynamic polarization curves display a typical pseudo-passivation behavior, along with clearly defined regions of passivation in each of the samples. These findings align with the electrochemical behavior of TiCN -based materials reported in studies conducted by Kumar et al. [56] and Mekgwe et al. [23]. The appearance of the passive region first on the polarization curves after reaching the critical current density is denoted as the first passive region. At higher anodic regions, the second passive region can be observed for all the composites in the three acidic solutions. The results also demonstrate the tendency of each sample to passivate, and in some cases, repassivation occurs. Repassivation is more evident in specimens A and B in the HCl solution, while C and D exhibited higher repassivation than the other specimens in the sulfuric acid electrolyte. However, specimen A shows a rapid increase in current density with increased potential, which indicates rapid dissolution of the specimen because of aggressive chloride ions present in the electrolyte. The addition of graphite reinforcement is seen to enhance the formation of oxide layers on the surface of the specimens. These layers provide temporary protection for the specimens, thereby reducing the effect of ion attack during the test.

According to Fig. 13, an increase in potential is apparent, which

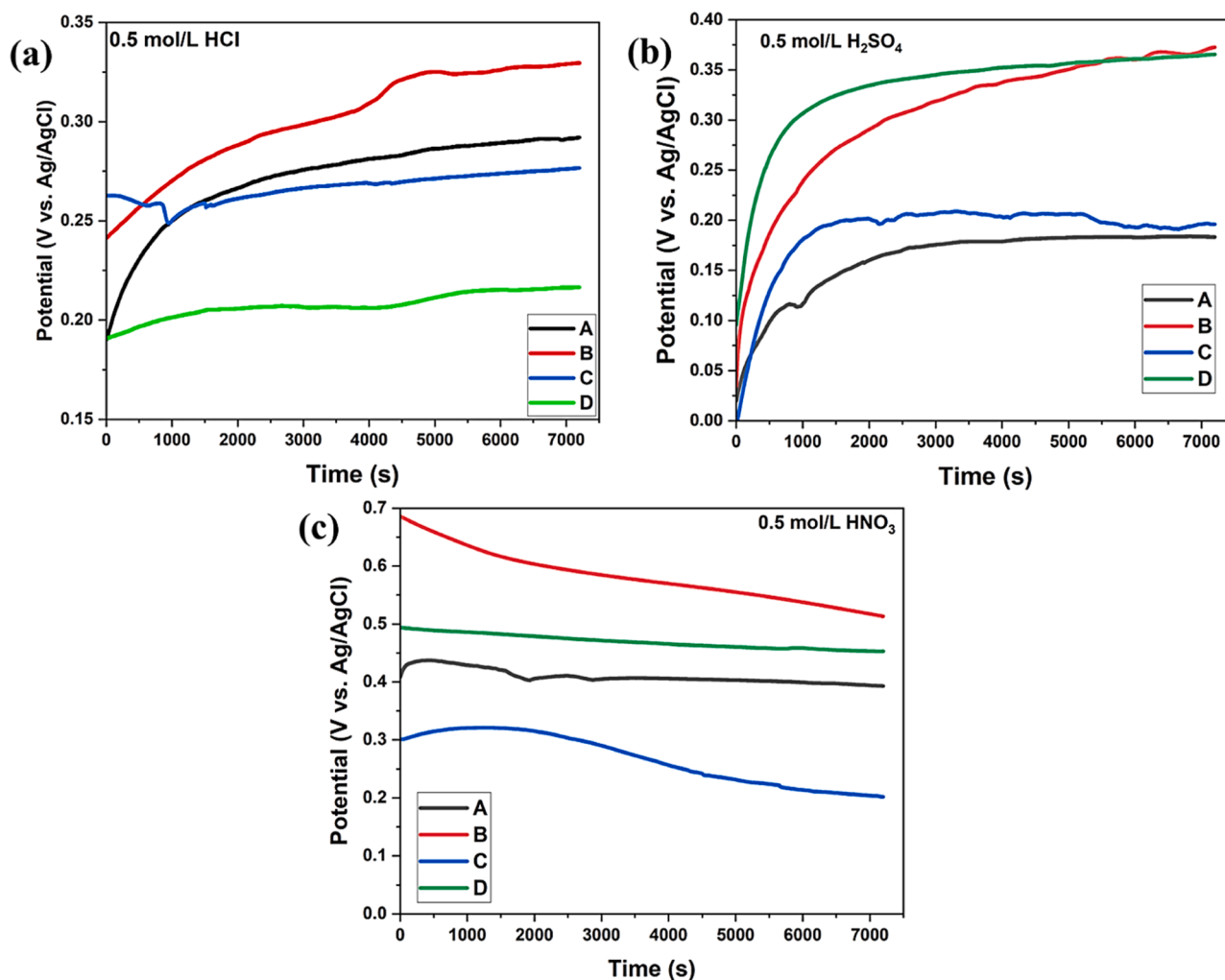


Fig. 12. Open circuit potential plot for TiCN-Gr ceramic composites after 2 h immersion time in test electrolytes, (a) HCl (b) H_2SO_4 and (c) HNO_3 solutions.

denotes that these specimens have enhanced corrosion resistance in the electrolyte. For the HCl test solution, specimen A recorded an E_{corr} value of 497.06 mV. With the addition of 0.5 wt% graphite content (B), the value decreased to 376.72 mV, which is lesser than the value recorded for specimen A. However, an increase in graphite content to 1.0 and 1.5 wt% increased the E_{corr} values to 579.6 and 522.9 mV, respectively. It can be further observed that the E_{corr} of TiCN-Gr composites decreased with lower content of graphite addition and significantly increased at 1.0 and 1.5 wt% of graphite addition in 0.5 mol/L HCl solution. The resistance to corrosion could be associated with the residual porosity of the specimen, and for this study, the specimen with lower porosity (refer to Table 2) is believed to reduce the penetration of the aggressive electrolyte into the specimen surface, thereby reducing susceptibility to pitting corrosion. In general, the current density illustrates the kinetics driving force and the degree of electrochemical corrosion of the specimens. The composites with decreased current density exhibit high corrosion resistance in the immersed electrolyte. It should be noted that although there is a tendency to corrode, all the specimens have demonstrated I_{corr} values that are significantly low, suggesting that the composites have an overall ability to withstand corrosion. Based on this study, ceramic composite with enhanced corrosion resistance is shown in specimen B (0.452 μA) as compared to the current densities of 2.336 μA , 5.065 μA , and 16.835 μA exhibited by A, C, and D respectively, in HCl solution. Observing the electrochemical parameters for H_2SO_4 solution, specimen A has a lower current density value of 0.041 μA , and in HNO_3 solution, the specimen with 1.0 wt% graphite

content (specimen C) exhibited a current density of 0.081 μA . Excess graphite addition has shown higher I_{corr} values of 16.835 μA , 3.08 μA and 0.525 in HCl, H_2SO_4 and HNO_3 solutions respectively. This proves that excess graphite content does not enhance corrosion resistance of the composites due to the large pores caused by undissolved graphite. The lower quantity of graphite reinforcement (0.5 and 1.0 wt%) refines the microstructure and delays the corrosion of the substrate. Similar observation was reported in studies where ruthenium [19] and WC [53] were as used to enhance the corrosion resistance of TiCN-based materials; although only a small quantity of reinforcement enhanced the corrosion properties, while an excess quantity deteriorated the corrosion properties due to presence porosities in the specimens.

The corrosion resistance of TiCN-Gr composites was additionally investigated using electrochemical impedance spectroscopy (EIS) technique and the results are illustrated using Nyquist and bode plots presented in Figs. 14 and 15 respectively. Furthermore, the EIS fitting parameters for TiCN-Gr composites immersed in 0.5 mol/L HCl, H_2SO_4 and HNO_3 acidic solutions are presented in Table 4. It is noteworthy that the interface between the electrolyte and the specimen does not work like a perfect capacitor, therefore modelling the interface with constant phase element (CPE) was suitable. The EIS data obtained by Z-view software (version 4.0 h) to evaluate the impedance spectra is summarized in Table 4 and the equivalent circuit was used to provide parameters such as electrolyte resistance (R_1) between the working electrode and the reference electrode. The corrosion interface is illustrated by a parallel capacitor comprised of a double layer constant phase element

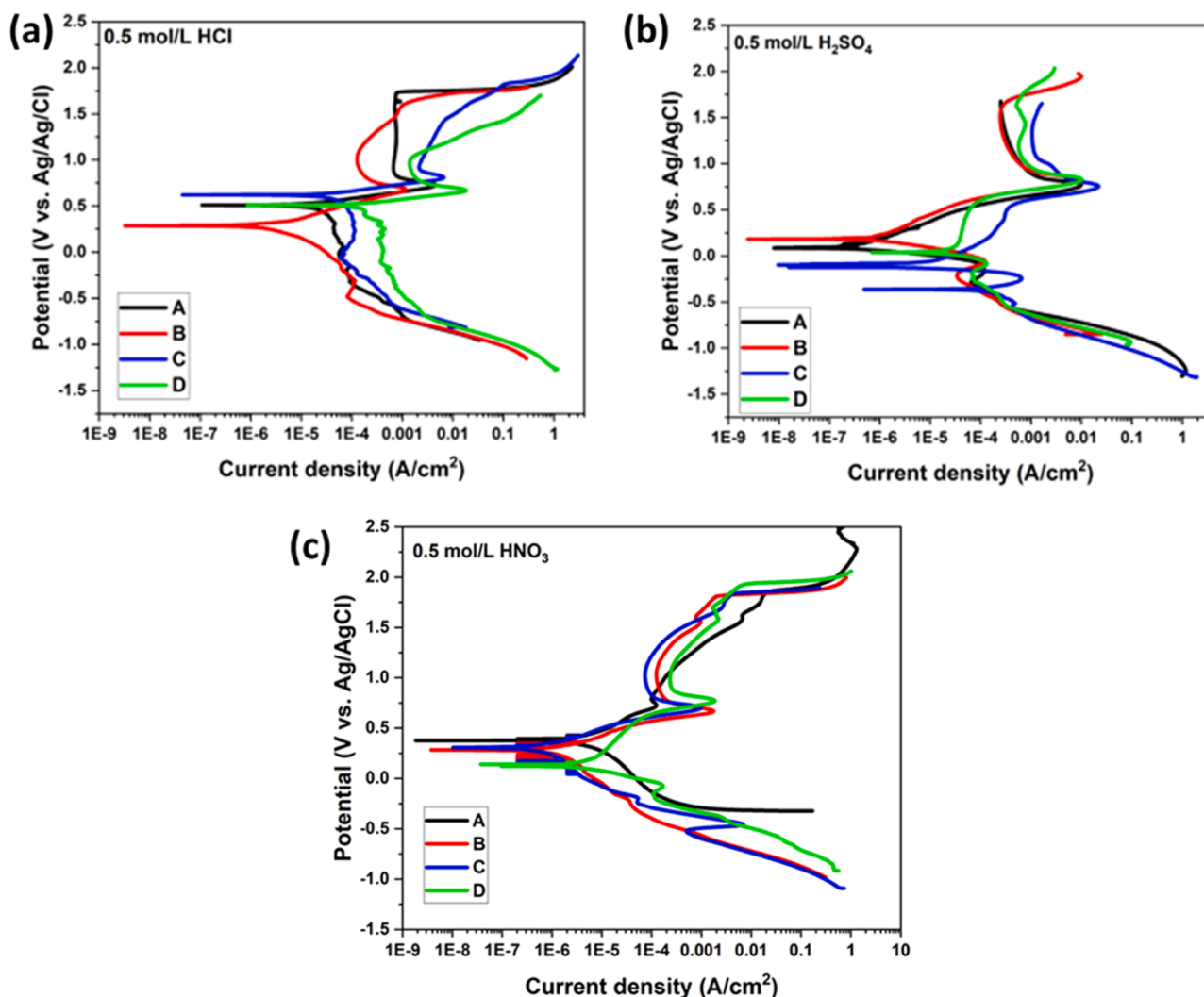


Fig. 13. Potentiodynamic polarization curves of TiCN-Gr composites in test electrolytes, (a) HCl (b) H₂SO₄ and (c) HNO₃ solutions.

Table 3

Electrochemical parameters from Tafel fitting of the potentiodynamic polarization curves.

Electrolyte	Sample ID	E _{corr} (mV)	I _{corr} (μA)	Cathodic beta (mV)	Anodic beta (mV)
HCl	A	497.06	2.336	404.708	87.106
	B	376.72	0.452	371.573	124.772
	C	579.6	5.065	137.103	108.744
	D	522.9	16.835	484.034	36.921
H ₂ SO ₄	A	131.09	0.041	73.1	181.74
	B	227.62	0.161	118.537	235.743
	C	-102.91	1.656	52.139	300.535
	D	78.831	3.08	209.156	583.458
HNO ₃	A	411.05	0.478	328.513	180.987
	B	285.54	0.146	357.538	134.597
	C	306.24	0.081	379.68	143.322
	D	145.03	0.525	120.467	335.185

(CPE) and a charge transfer resistance (R_p) to analyze the EIS fit data is represented in Fig. 16. It is evident from Fig. 14 that various impedance behaviours with different capacitive arc radii exist across the ceramic composites in the three electrolytes. Characteristically, the increase in the diameter of the arc designates enhancement of the film and charge transfer resistance of the material in the corrosive media. Fig. 14a demonstrated higher impedance in specimen B, which clearly indicates higher corrosion resistance to aggressive chloride ions as compared to

specimens A, C and D. This behaviour could be attributed to the formation of passive resistant layer stimulated by carbon addition into the composite. With the EIS results represented in Fig. 14b, it can be observed that the impedance of specimen A is higher than B, C and D, which further indicates that graphite content does not have an effect on the corrosion resistance of TiC₇₀N₃₀ composites in the H₂SO₄ electrolyte. However, specimen C shows higher corrosion resistance. An enhancement of the film and charge transfer resistance is ascribed to the increase in the arc diameter. [59]. A similar observation was reported in a study by Chen et al. [16], whereby TiCN cermet without Cr content showed a semi-circle shape as compared to other cermets which exhibited 45° line influenced by the presence of the chromium in 0.2 mol/L H₂SO₄ test solution.

An increase in diameter of the arc strongly indicates the formation of passive film while small capacitive arc radii at the high frequency of the material are ascribed to the porous external layer and interconnected pores in the specimen [60]. Two capacitive arcs can be assigned to the different resistance and capacitance behaviour, at high frequency, transformation of corrosion electrons into the electrolyte interface by the pores occurs [61]. This short capacitance-like behaviour is due to electrons passing through the working electrode interface, and this clearly corresponds to specimen D in Fig. 14c due to presence of pores in it. The bode plots of TiCN-Gr composites shown in Fig. 15 demonstrate a wide phase angle plateau over an intermediate range of frequency (1–100 Hz) corresponding to the log |Z| and log frequency which

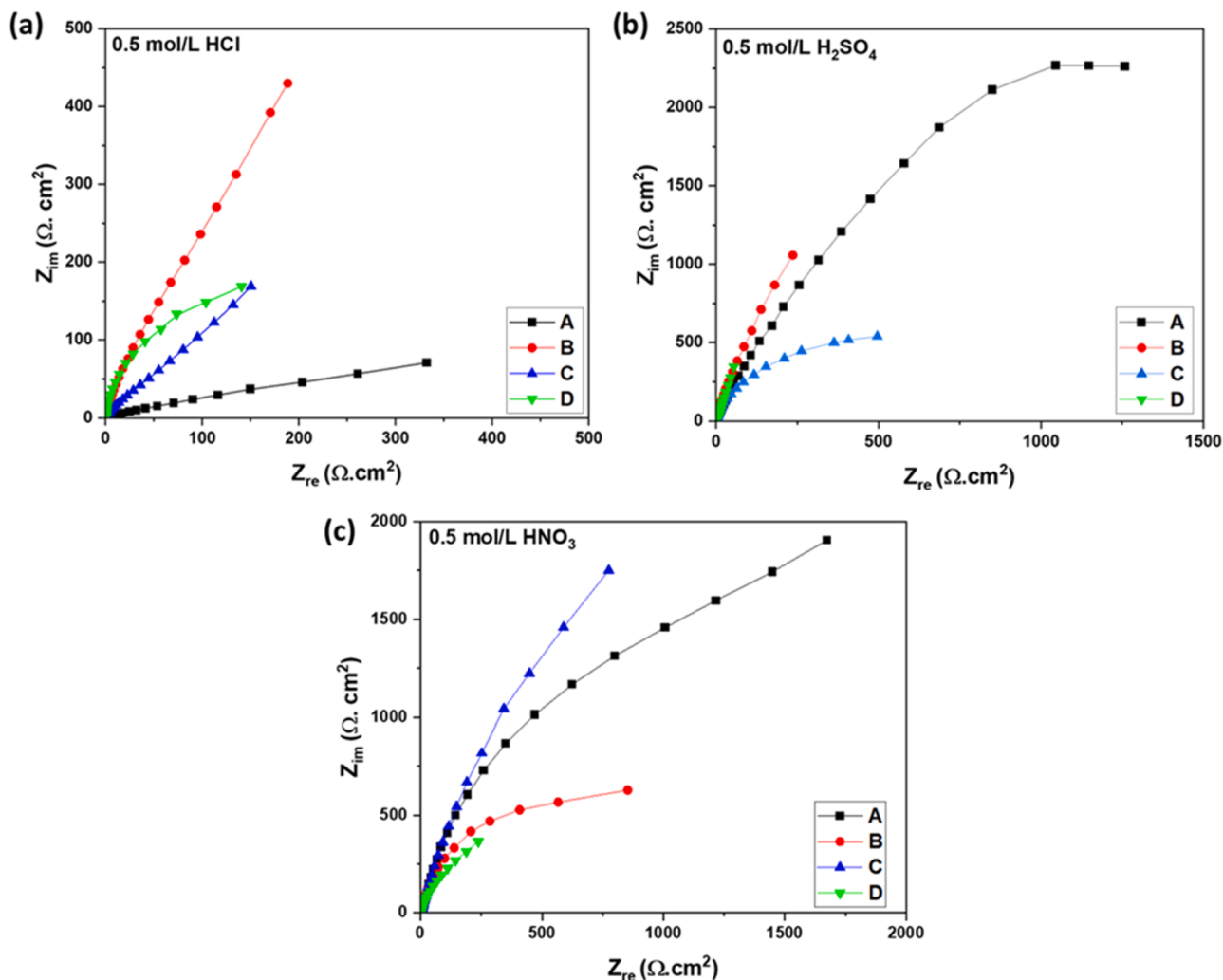


Fig. 14. Nyquist electrochemical impedance spectroscopy (EIS) measurement plots of TiCN-Gr composites in test electrolytes, (a) HCl (b) H₂SO₄ and (c) HNO₃ solutions.

indicates a well-linear variation. These plots signify superior capacitive attributes of these composites which further impedes the penetration of the electrolyte during exposure in the test solution. Typically, the greater slope represents the smaller impedance of diffusion ions at the interface while the impedance at high frequency is characterized by layer resistance [62]. From Fig. 15, it can be seen that the phase angles achieved in the passive region showed a peak value in the range of -70° to -80° over the low and middle frequency range (0.1–100 Hz) owing to a pronounced stable passive film formation followed by a rapid decrease towards 0° in the high frequency zone indicating electrolyte resistance dominance. Higher impedance modulus is observed for ceramic composite B, A and both A and C in HCl, H₂SO₄ and HNO₃ electrolytes respectively and these findings corroborates with I_{corr} values represented in Table 3. The high-frequency impedance correlates to the characteristics of the formation of corrosion products on TiCN-Gr surface throughout the electrochemical reaction in acidic electrolytes. In H₂SO₄ solution, graphite proved to have insignificant influence on the TiCN composites. Hence, ceramic composite without graphite addition exhibited enhanced corrosion resistance as compared to TiCN-Gr composites. From this study, it is evident that adequate addition of graphite content (0.5 and 1.0 wt%) into the TiCN matrix is beneficial in enhancing the corrosion resistance of the composites in HCl and HNO₃ electrolytes. Overall, specimens with 0.5 wt% graphite addition performed well and demonstrated enhanced corrosion resistance in all the acidic solutions, predominantly in the 0.5 mol/L HCl solution.

4. Conclusion

The influence of sintering parameters on the densification and corrosion properties of TiCN-Gr composites was investigated. Furthermore, the effect of varying graphite additions on the corrosion resistance of the TiCN composites was also investigated. The following key findings are noted from this study:

- Novel sintering technology has proven successful in consolidating highly dense graphite reinforced pure TiCN ceramic composites. Displacement increased with rising sintering temperature, indicating enhanced diffusion mechanism and mass transportation between graphite and TiC70N30 powder particles during sintering.
- Relative densities up to 97.8 % and 99.6 % for sintered composites with 0.5 % and 1 % graphite addition were achieved. The decreased relative density observed in 1.5 wt% graphite reinforcement was attributed to the presence of pores as seen in the SEM micrographs.
- The composites reinforced with adequate amount of graphite showed enhanced resistance to corrosion in the HCl and HNO₃ acidic electrolytes due to the inability of aggressive ions to adequately attack the specimen surface owing to the formation of protective oxide layers. In H₂SO₄ electrolyte, ceramic composite without graphite reinforcement showed enhanced corrosion resistance as compared to other specimens.

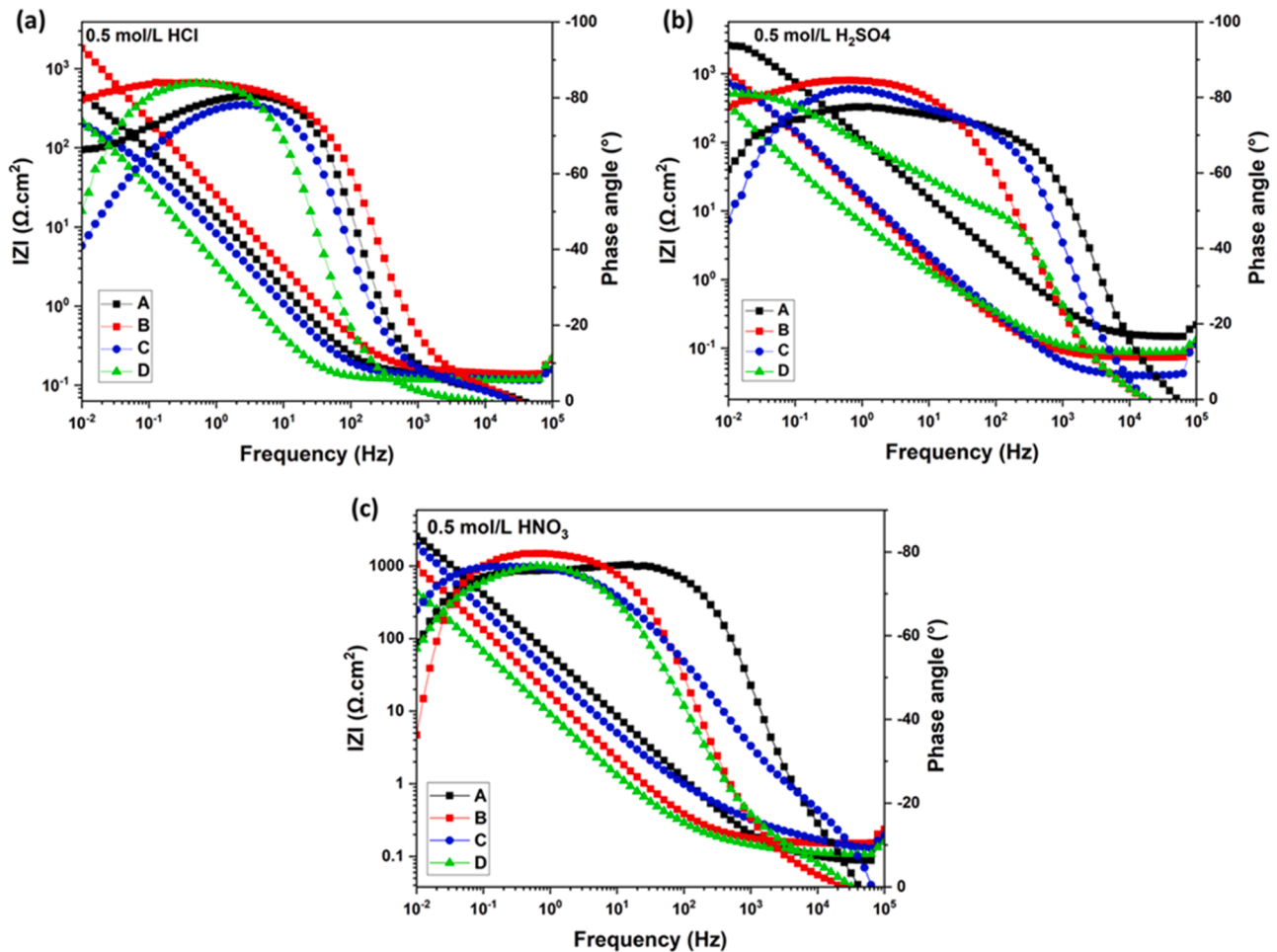


Fig. 15. Bode plots of TiCN-Gr composites in test electrolytes, (a) HCL (b) H₂SO₄ and (c) HNO₃ solutions.

Table 4
EIS fitting parameters for TiCN-Gr composites.

Electrolyte	Sample ID	Rs (Ω cm ²)	CPE1 T (mF/cm ²) × 10 ⁻³	Rp (Ω cm ²)
HCl	A	1.363	1.310	2069
	B	1.479	0.752	1.559E11
	C	1.164	4.573	2029
	D	1.182	5.084	1.356E15
H ₂ SO ₄	A	1.434	0.5381	5.512E13
	B	0.7702	1.3187	8.832E10
	C	0.3956	1.181	5.1638E14
	D	0.8117	4.1475	1.4863E10
HNO ₃	A	4.92	37.978	2.0943E09
	B	1.613	1.195	3.005E20
	C	1.698	0.9934	8.7822E10
	D	1.215	2.7496	1E20



Fig. 16. Equivalent circuit used for EIS curve fitting.

- Excess graphite content does not improve corrosion resistance of the composites due to the large pores caused by undissolved graphite. The lower quantity of graphite reinforcement (0.5 and 1.0 wt%) refines the microstructure and delays the corrosion course of the substrate.

- The corrosion behaviour was characterized by a parallel capacitor with a double layer constant phase element and a charge transfer.

CRediT authorship contribution statement

Peter Apata Olubambi: Funding acquisition, Resources, Supervision, Visualization. **Gadifele Nicolene Mekgwe:** Conceptualization, Investigation, Methodology, Writing – original draft. **Samuel Olukayode Akinwamide:** Investigation, Project administration, Supervision, Validation, Visualization, Writing – review & editing. **Ojo Jeremiah Akinribide:** Conceptualization, Investigation, Methodology, Project administration.

Declaration of Competing Interest

The authors declare that they have no known competing financial interests or personal relationships that could have appeared to influence the work reported in this paper.

Acknowledgement

The authors are grateful to National Research Foundation of South Africa for providing funding for this research.

References

[1] P. Ettmayer, H. Kolaska, W. Lengauer, K. Dreyer, Ti(C,N) cermets — Metallurgy and properties, Int J. Refract Met. Hard Mater. 13 (6) (1995) 343–351, [https://doi.org/10.1016/0263-4368\(95\)00027-G](https://doi.org/10.1016/0263-4368(95)00027-G).

- [2] H.M. Ortner, P. Ettmayer, H. Kolaska, The history of the technological progress of hardmetals, *Int J. Refract Met. Hard Mater.* 44 (2014) 148–159, <https://doi.org/10.1016/j.ijrmhm.2013.07.014>.
- [3] Y. Peng, H. Miao, Z. Peng, Development of TiCN-based cermets: Mechanical properties and wear mechanism, *Int J. Refract Met. Hard Mater.* 39 (2013) 78–89, <https://doi.org/10.1016/j.ijrmhm.2012.07.001>.
- [4] E. Shankar, S.B. Prabu, K.A. Padmanabhan, Mechanical properties and microstructures of TiCN/nano-TiB₂/TiN cermets prepared by spark plasma sintering, *Ceram. Int.* 44 (8) (2018) 9384–9394, <https://doi.org/10.1016/j.ceramint.2018.02.154>.
- [5] O.J. Akinribide, et al., Sintering of binderless TiN and TiCN-based cermet for toughness applications: processing techniques and mechanical properties: a review, *Ceram. Int.* 45 (17) (2019) 21077–21090, <https://doi.org/10.1016/j.ceramint.2019.07.191>.
- [6] L. Zhang, Q. Ling, J. Gu, Z. Zhong, J. Long, C. Wang, Strengthening and toughening of Ti(C,N)-based cermets: (Ti,W)C additive design and the mechanism, *Int J. Refract Met. Hard Mater.* 103 (2022) 105758, <https://doi.org/10.1016/j.ijrmhm.2021.105758>.
- [7] H. Hosokawa, K. Shimojima, A. Matsumoto, K. Kato, H. Matsubara, Wettability of Ni/(Ti_xMe_{1-x})(CuNv) System (Me=Mo, W), *Int J. Refract Met. Hard Mater.* vol. 33 (Jul. 2012) 1–5, <https://doi.org/10.1016/j.ijrmhm.2012.01.005>.
- [8] A.J. Ruys, Cemented carbides and cermets, in: *Metal-Reinforced Ceramics*, Elsevier, 2021, pp. 285–325, <https://doi.org/10.1016/B978-0-08-102869-8.00008-2>.
- [9] H. Li, et al., TiCN nanoparticle-induced corrosion inhibition mechanisms of AZ91 alloy, *Corros. Sci.* 198 (2022) 110109, <https://doi.org/10.1016/j.corsci.2022.110109>.
- [10] Y. Sun, et al., Nanomechanical properties of TiCN and TiCN/Ti coatings on Ti prepared by filtered arc deposition, *Mater. Sci. Eng.: A* vol. 625 (2015) 56–64, <https://doi.org/10.1016/j.msea.2014.11.093>.
- [11] F. Zhang, J. He, K. Chen, Y. Qin, C. Li, F. Yin, Microstructure evolution and mechanical properties of TiCN-Cr nano/micro composite coatings prepared by reactive plasma spraying, *Appl. Surf. Sci.* 427 (2018) 905–914, <https://doi.org/10.1016/j.apsusc.2017.08.121>.
- [12] F. Zhang, C. Li, S. Yan, J. He, B. Liu, F. Yin, Microstructure and tribological properties of plasma sprayed TiCN-Mo based composite coatings, *Appl. Surf. Sci.* 464 (2019) 88–98, <https://doi.org/10.1016/j.apsusc.2018.09.063>.
- [13] P. Alvaredo, E. Gordo, O. Van der Biest, K. Vanmeensel, Microstructural development and mechanical properties of iron based cermets processed by pressureless and spark plasma sintering, *Mater. Sci. Eng.: A* 538 (2012) 28–34, <https://doi.org/10.1016/j.msea.2011.12.107>.
- [14] P. Alvaredo, J.J. Roa, E. Jiménez-Pique, L. Llanes, E. Gordo, Characterization of interfaces between TiCN and iron-base binders, *Int J. Refract Met. Hard Mater.* 63 (2017) 32–37, <https://doi.org/10.1016/j.ijrmhm.2016.08.010>.
- [15] V. Verma, B.V.M. Kumar, Sliding wear behavior of SPS processed TaC-containing Ti(CN)-WC-Ni/Co cermets against Silicon Carbide, *Wear* 376–377 (2017) 1570–1579, <https://doi.org/10.1016/j.wear.2017.02.013>.
- [16] S. Chen, et al., Corrosion behavior of Ti(C,N)-Ni/Cr cermets in H₂SO₄ solution, *Int J. Refract Met. Hard Mater.* 47 (2014) 139–144, <https://doi.org/10.1016/j.ijrmhm.2014.07.010>.
- [17] S. Park, Y.J. Kang, H.J. Kwon, S. Kang, Synthesis of (Ti,M₁M₂)(CN)-Ni nanocrystalline powders, *Int J. Refract Met. Hard Mater.* 24 (1–2) (2006) 115–121, <https://doi.org/10.1016/j.ijrmhm.2005.05.002>.
- [18] B. Walther, J. Schilm, A. Michaelis, M.M. Lohrengel, Electrochemical dissolution of hard metal alloys, *Electrochim. Acta* 52 (2007) 7732–7737, <https://doi.org/10.1016/j.electacta.2006.12.038>.
- [19] L.W. Xu, N. Lin, L.B. Zhao, C. Ma, Z.Y. Wang, Y.H. He, Effect of Ni contents on mechanical properties and corrosion behavior of Ti(C,N)-WC-Mo₂C-(Ni,Co) cermets, *Mater. Chem. Phys.* 252 (2020) 123253, <https://doi.org/10.1016/j.matchemphys.2020.123253>.
- [20] L. Zhao, N. Lin, Y. He, Improvement in microstructure and properties of Ti(C,N)-based cermets with Ruthenium additions, *Ceram. Int.* 44 (14) (2018) 17553–17561, <https://doi.org/10.1016/j.ceramint.2018.06.156>.
- [21] W. Wan, J. Xiong, M. Yang, Z. Guo, G. Dong, C. Yi, Effects of Cr₃C₂ addition on the corrosion behavior of Ti(C, N)-based cermets, *Int. J. Refract Met. Hard Mater.* 31 (2012) 179–186, <https://doi.org/10.1016/j.ijrmhm.2011.10.013>.
- [22] M. Zhang, N. Lin, Y. He, X. Kang, A comparative study on microstructure and properties of Ti(C,N)-based cermets with the various Cr doping methods, *J. Alloy. Compd.* 799 (2019) 462–473, <https://doi.org/10.1016/j.jallcom.2019.05.159>.
- [23] V.A. Lavrenko, A.D. Panasyuk, M. Desmaison-Brut, V.A. Shvets, J. Desmaison, Kinetics and mechanism of electrolytic corrosion of titanium-based ceramics in 3% NaCl solution, *J. Eur. Ceram. Soc.* 25 (10) (2005) 1813–1818, <https://doi.org/10.1016/j.jeurceramsoc.2004.12.014>.
- [24] G.N. Mekgwe, S.O. Akinwamide, O.J. Akinribide, P.A. Olubambi, Insight into tribological and corrosion behaviour of binderless TiC_xN_y ceramic composites processed via pulsed electric current sintering technique, *Ceram. Int.* 48 (17) (2022) 24793–24802, <https://doi.org/10.1016/j.ceramint.2022.05.129>.
- [25] D.E. Wolfe, et al., Influence of processing on the microstructural evolution and multiscale hardness in titanium carbonitrides (TiCN) produced via field assisted sintering technology, *Materialia* 27 (2023) 101682, <https://doi.org/10.1016/j.mtla.2023.101682>.
- [26] F. Guillard, A. Allemand, J.-D. Lulewicz, J. Galy, Densification of SiC by SPS-effects of time, temperature and pressure, *J. Eur. Ceram. Soc.* 27 (7) (2007) 2725–2728, <https://doi.org/10.1016/j.jeurceramsoc.2006.10.005>.
- [27] O. Zgalat-Lozynskyy, M. Herrmann, A. Ragulya, Spark plasma sintering of TiCN nanopowders in non-linear heating and loading regimes, *J. Eur. Ceram. Soc.* 31 (5) (2011) 809–813, <https://doi.org/10.1016/j.jeurceramsoc.2010.11.030>.
- [28] S. Diouf, A. Molinari, Densification mechanisms in spark plasma sintering: effect of particle size and pressure, *Powder Technol.* 221 (2012) 220–227, <https://doi.org/10.1016/j.powtec.2012.01.005>.
- [29] O.E. Falodun, B.A. Obadele, S.R. Oke, O.O. Ige, P.A. Olubambi, Effect of TiN and TiCN additions on spark plasma sintered Ti–6Al–4V, *Part. Sci. Technol.* 38 (2) (2020) 156–165, <https://doi.org/10.1080/02726351.2018.1515798>.
- [30] E. Ghasali, H. Nouranian, A. Rahbari, H. Majidian, M. Alizadeh, T. Ebadzadeh, Low temperature sintering of aluminum-zircon metal matrix composite prepared by spark plasma sintering, *Mater. Res. Res.* 19 (5) (2016) 1189–1192, <https://doi.org/10.1590/1980-5373-MR-2016-0395>.
- [31] A.S. Hakeem, et al., Comparative evaluation of thermal and mechanical properties of nickel alloy 718 prepared using selective laser melting, spark plasma sintering, and casting methods, *J. Mater. Res. Technol.* 12 (2021) 870–881, <https://doi.org/10.1016/j.jmrt.2021.03.043>.
- [32] H. Wang, Graphite solid lubrication materials, in: *Encyclopedia of Tribology*, Springer US, Boston, MA, 2013, pp. 1550–1555, https://doi.org/10.1007/978-0-387-92897-5_1261.
- [33] N. Saheb, et al., Spark plasma sintering of metals and metal matrix nanocomposites: a review, *J. Nanomater* 2012 (2012) 1–13, <https://doi.org/10.1155/2012/983470>.
- [34] A. Borrell, M.D. Salvador, V. García-Rocha, A. Fernández, E. Chicardi, F.J. Gotor, Spark plasma sintering of Ti_yNb_{1-y}CxN_{1-x} monolithic ceramics obtained by mechanically induced self-sustaining reaction, *Mater. Sci. Eng.: A* 543 (2012) 173–179, <https://doi.org/10.1016/j.msea.2012.02.071>.
- [35] P. Tatarco, S. Grasso, T.G. Saunders, V. Casalegno, M. Ferraris, M.J. Reece, Flash joining of CVD-SiC coated Cf/SiC composites with a Ti interlayer, *J. Eur. Ceram. Soc.* 37 (13) (2017) 3841–3848, <https://doi.org/10.1016/j.jeurceramsoc.2017.05.016>.
- [36] A. Babapoor, M.S. Asl, Z. Ahmadi, A.S. Namini, Effects of spark plasma sintering temperature on densification, hardness and thermal conductivity of titanium carbide, *Ceram. Int.* 44 (12) (2018) 14541–14546, <https://doi.org/10.1016/j.ceramint.2018.05.071>.
- [37] G. Liu, R. Li, T. Yuan, M. Zhang, F. Zeng, Spark plasma sintering of pure TiCN: Densification mechanism, grain growth and mechanical properties, *Int J. Refract Met. Hard Mater.* 66 (2017) 68–75, <https://doi.org/10.1016/j.ijrmhm.2017.02.008>.
- [38] O.J. Akinribide, G.N. Mekgwe, O.O. Ajibola, B.A. Obadele, S.O. Akinwamide, P. A. Olubambi, Studies on mechanical properties of graphite reinforced Ti (Cx, N1-x) using nanoindentation techniques, *Procedia Manuf.* (2019), <https://doi.org/10.1016/j.promfg.2019.02.085>.
- [39] B.M. Moshtaghion, J.M. Morgado Chávez, F.L. Cumbreira, D. Gómez García, Titanium carbonitride fabricated by spark plasma sintering: Is it a ceramic model of carbon-induced Friedel-Fleisher strengthening effect? *J. Eur. Ceram. Soc.* 41 (13) (2021) 6275–6280, <https://doi.org/10.1016/j.jeurceramsoc.2021.06.039>.
- [40] Y. Li, N. Liu, X. Zhang, C. Rong, Effect of carbon content on the microstructure and mechanical properties of ultra-fine grade (Ti,W) (C,N)-Co cermets, *J. Mater. Process Technol.* 206 (1–3) (2008) 365–373, <https://doi.org/10.1016/j.jmatprotec.2007.12.086>.
- [41] W. Lengauer, F. Scagnetto, Ti(C,N)-based cermets: critical review of achievements and recent developments, *Solid State Phenom.* 274 (2018) 53–100, <https://doi.org/10.4028/www.scientific.net/SSP.274.53>.
- [42] Y. Zhao, Y. Zheng, W. Zhou, J. Zhang, Q. Huang, W. Xiong, Effect of carbon addition on the densification behavior, microstructure evolution and mechanical properties of Ti(C, N)-based cermets, *Ceram. Int.* 42 (4) (2016) 5487–5496, <https://doi.org/10.1016/j.ceramint.2015.12.097>.
- [43] M. Chen, Q. Zhuang, N. Lin, Y. He, Improvement in microstructure and mechanical properties of Ti(C,N)-Fe cermets with the carbon additions, *J. Alloy. Compd.* 701 (2017) 408–415, <https://doi.org/10.1016/j.jallcom.2017.01.119>.
- [44] O.J. Akinribide, G.N. Mekgwe, B.A. Obadele, O.O. Ajibola, S.O. Akinwamide, P. A. Olubambi, Microstructural and phase evolution of spark plasma sintering of graphitized Ti (C_{0.9}N_{0.1}) composites, *Int. J. Refract. Met. Hard Mater.* 78 (2019) 164–169, <https://doi.org/10.1016/j.ijrmhm.2018.09.013>.
- [45] Z. Wang, et al., Carburization and wear behavior of self-lubricating Ti(C,N)-based cermets with various secondary carbides, *Ceram. Int.* 47 (19) (2021) 26678–26691, <https://doi.org/10.1016/j.ceramint.2021.06.075>.
- [46] O.J. Akinribide, et al., The role of graphite addition on spark plasma sintered titanium nitride, *J. Mater. Res. Technol.* 9 (3) (2020) 6268–6277, <https://doi.org/10.1016/j.jmrt.2020.03.040>.
- [47] S. Zhou, Z. Wang, W. Zhang, Effect of graphite flake orientation on microstructure and mechanical properties of ZrB₂-SiC-graphite composite, *J. Alloy. Compd.* 485 (1–2) (2009) 181–185, <https://doi.org/10.1016/j.jallcom.2009.05.126>.
- [48] S. ZHOU, J. TAN, W. PENG, S. WANG, P. LI, Sintering technology of Ti(C, N) base cermets, *Trans. Nonferrous Met. Soc. China* 19 (2009) s696–s700, [https://doi.org/10.1016/S1003-6326\(10\)60134-3](https://doi.org/10.1016/S1003-6326(10)60134-3).
- [49] Y. Li, N. Liu, X. Zhang, C. Rong, Effect of carbon content on the microstructure and mechanical properties of ultra-fine grade (Ti,W) (C,N)-Co cermets, *J. Mater. Process Technol.* 206 (1–3) (2008) 365–373, <https://doi.org/10.1016/j.jmatprotec.2007.12.086>.
- [50] Y. Qin, H. Zhao, C. Li, J. Lu, J. He, Effect of heat treatment on the microstructure and corrosion behaviors of reactive plasma sprayed TiCN coatings, *Surf. Coat. Technol.* 398 (2020) 126086, <https://doi.org/10.1016/j.surfcoat.2020.126086>.

- [51] H.S. Gujral, et al., Mesoporous titanium carbonitride derived from mesoporous C3N5 for highly efficient hydrogen evolution reaction, *Carbon N. Y.* 195 (2022) 9–18, <https://doi.org/10.1016/j.carbon.2022.03.060>.
- [52] K. Liang, et al., Two-dimensional titanium carbonitride MXene as a highly efficient electrocatalyst for hydrogen evolution reaction, *Mater. Rep.: Energy* 2 (1) (2022) 100075, <https://doi.org/10.1016/j.matre.2021.100075>.
- [53] V.A. Lavrenko, V.A. Shvets, V.N. Talash, Electrolytic corrosion of titanium carbonitride composites, *Powder Metall. Met. Ceram.* 43 (1/2) (2004) 62–66, <https://doi.org/10.1023/B:PMMC.0000028273.86448.54>.
- [54] G.S. Frankel, *Fundamentals of Corrosion Kinetics*, 2016, pp. 17–32, [10.1007/978-94-017-7540-3_2](https://doi.org/10.1007/978-94-017-7540-3_2).
- [55] N. Botshekanan, H. Majidian, M. Farvizi, Corrosion behavior of TiN and TiCN coatings synthesized by PVD on the spark plasma sintered NiTi substrate, *Synth. Sinter.* 3 (3) (2023) 158–165, <https://doi.org/10.53063/synsint.2023.33166>.
- [56] H. Kwon, S. Kang, Stability domain of Ti(CN) in Ti–TiC–TiN, *Mater. Lett.* 68 (2012) 426–428, <https://doi.org/10.1016/j.matlet.2011.11.030>.
- [57] A. Rajabi, et al., Challenges and solutions in the synthesis of nano-TiCN: a review, *Ceram. Int.* 48 (7) (2022) 8921–8929, <https://doi.org/10.1016/j.ceramint.2021.12.366>.
- [58] G. Zheng, X. Gao, Z. Xing, H. Hong, Z. Ju, “Tremella-shaped TiCN Nanosheets as Anode Materials of Lithium-Ion Batteries, *ChemistrySelect* 5 (43) (2020) 13502–13510, <https://doi.org/10.1002/slct.202002957>.
- [59] L. Zhang, Y. Feng, Q. Nan, R. Ke, Q. Wan, Z. Wang, Effects of titanium-based raw materials on electrochemical behavior of Ti(C,N)-based cermets, *Int. J. Refract. Met. Hard Mater.* 48 (2015) 11–18, <https://doi.org/10.1016/j.ijrmhm.2014.07.019>.
- [60] Y. Chen, J. Xu, S. Jiang, Z.-H. Xie, P. Munroe, S. Kuai, Corrosion-resistant, electrically conductive TiCN coatings for direct methanol fuel cell, *Surf. Coat. Technol.* 422 (2021) 127562, <https://doi.org/10.1016/j.surfcoat.2021.127562>.
- [61] T.S. Tshephe, S.O. Akinwamide, M.J. Phala, E. Olevsky, P.A. Olubambi, Structural characterization and biocorrosion behaviour of direct metal laser sintered Ti6Al4V–ZrO2 tracks: Influence of processing parameters, *Results Mater.* 13 (2022) 100257, <https://doi.org/10.1016/j.rinma.2022.100257>.
- [62] D.D. Macdonald, Reflections on the history of electrochemical impedance spectroscopy, *Electrochim. Acta* 51 (8–9) (2006) 1376–1388, <https://doi.org/10.1016/j.electacta.2005.02.107>.